

# Recent Advances in Synthesis and Study of 2D Twisted Transition Metal Dichalcogenide Bilayers

Bijun Tang, Bingyu Che, Manzhang Xu, Zhi Peng Ang, Jun Di, Hong-Jun Gao, Haitao Yang,\* Jiadong Zhou,\* and Zheng Liu\*

In recent years, twisted 2D transition metal dichalcogenides (TMDs) have attracted tremendous research interest thanks to their intriguing properties that are essential in developing future electronic and photoelectronic devices in this modernizing era. The aim of this review is to introduce recent developments in the preparation of twisted TMD (t-TMD) bilayers, their properties investigated by photoluminescence (PL) spectroscopy, Raman spectroscopy, and other techniques, as well as the related distinctive physical phenomena. First, various strategies for synthesizing t-TMD bilayers via the two-step stacking method and one-step chemical vapor deposition method are reviewed. Then, the commonly used characterization techniques in probing the interlayer coupling between the twisted layers are introduced. Moreover, the intriguing physical properties associated with twisting such as interlayer excitons and correlated electronic phases are summarized. Last but not least, challenges and future research directions are briefly discussed in light of recent advances in the field.

due to their potential applications in various fields such as optics, electronics, and catalysis.<sup>[1–3]</sup> Numerous 2D materials have been developed in the past decade, ranging from insulators to superconductors. However, most of the works reported so far are limited to the monolayer sample, while overlooking the bilayers, though countless fascinating physical phenomena have been observed in the past few years.<sup>[4–6]</sup> For example, graphene bilayers and graphene/boron nitride (BN) heterobilayers are found to possess various intriguing physical properties such as Fermi velocity renormalization,<sup>[7]</sup> new van Hove singularities,<sup>[8,9]</sup> unconventional quantum Hall effects, and Hofstadter's butterfly pattern.<sup>[10–12]</sup> These can be attributed to the weak van der Waals (vdW) interaction between the two layers. The interlayer

## 1. Introduction

Since the first successful isolation of graphene from graphite in 2004, 2D materials have attracted considerable attention


coupling in graphene depends sensitively on the interlayer twist angle. In 2018, the “magic” angle of  $1.1^\circ$  in twisted bilayer graphene (TBG) was reported, which gives rise to exotic phenomena, including intrinsic unconventional superconductivity and correlated insulator states.<sup>[13,14]</sup> This groundbreaking finding immediately triggered substantial research interest in the study of twisted bilayer 2D materials.<sup>[15–18]</sup> We have looked into the related literature and completed the publication statistics, i.e., number of publications, as shown in **Figure 1a**. In recent years (from 2010 to 2020), publications concerning twisted bilayers have increased rapidly, especially after the report of TBG, showing a considerably growing interest.

B. Tang, Dr. M. Xu, Z. P. Ang, Dr. J. Di, Prof. J. Zhou, Prof. Z. Liu  
School of Materials Science and Engineering  
Nanyang Technological University  
Singapore 639798, Singapore  
E-mail: jdzhou@bit.edu.cn; z.liu@ntu.edu.sg

B. Che, Prof. H.-J. Gao, Prof. H. Yang  
Beijing National Laboratory for Condensed Matter Physics and Institute of Physics  
Chinese Academy of Sciences  
Beijing 100190, China  
E-mail: htyang@iphy.ac.cn

Prof. J. Zhou  
Key Lab of Advanced Optoelectronic Quantum Architecture and Measurement (Ministry of Education)  
Beijing Key Lab of Nanophotonics & Ultrafine Optoelectronic Systems, and School of Physics  
Beijing Institute of Technology  
Beijing 100081, China

Prof. Z. Liu  
CINTRA CNRS/NTU/THALES  
UMI 3288, Research Techno Plaza, 50 Nanyang Drive, Border X Block, Level 6, Singapore 637553, Singapore

 The ORCID identification number(s) for the author(s) of this article can be found under <https://doi.org/10.1002/ssstr.202000153>.

DOI: 10.1002/ssstr.202000153

As an indispensable member of the 2D family as well as a perfect complement to graphene, 2D transition metal dichalcogenides (TMDs) have long been the center of research attention.<sup>[3,19–22]</sup> Their popularity can mainly be attributed to three reasons: 1) 2D TMDs, with a generalized formula of  $\text{MX}_2$  (where M refers to a transition metal of groups 4–10 and X represents a chalcogen), exhibit versatile properties. 2) 2D TMDs have desirable structures similar to graphene, which consist of covalent bonding in the constituent layers and vdW interactions with neighboring layers, rendering them ideal for the exploration of monolayer or few-layer properties.<sup>[23]</sup> 3) Structures and properties of TMDs shared in common provide an additional degree of freedom to study and tailor the resulting properties of TMD heterostructures.<sup>[24–26]</sup> Development of twisted TMD (t-TMD) bilayers not only provides an ideal platform to study the fundamental physical problems such as the many-body

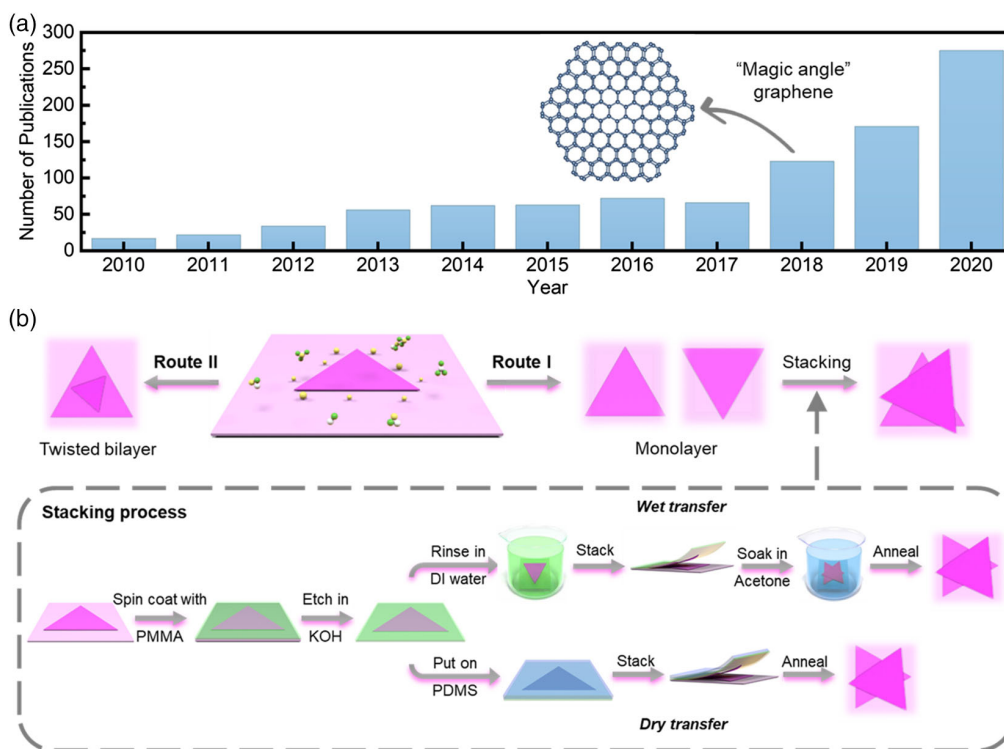


**Figure 1.** Overview of the recent study on twisted 2D materials. a) Publication trend regarding the study on twisted 2D bilayers from 2010 to 2020 (by Dec 29, 2020). Source: Web of Science. Search index: TOPIC: (twist) AND TOPIC: (bilayer). b) Schematic illustration of the preparation of t-TMD bilayers via stacking method (route I) and one-step CVD method (route II).

phenomenon,<sup>[27–30]</sup> but also promotes the realization of future electronic and photoelectronic devices.<sup>[31]</sup> Up to now, remarkable progress has been achieved with the study on t-TMDs bilayers, where ultrathin t-TMD bilayers have been successfully synthesized and the associated interlayer coupling has been systematically studied.<sup>[32–37]</sup> For instance, researchers have found out that the photoluminescence (PL) intensity ratio of the trion and the exciton of MoS<sub>2</sub> is highly dependent on the twist angle of bilayers.<sup>[32]</sup> To put it another way, twisting the stacking configuration of the bilayer is a promising method to alter the intrinsic properties of the materials.

To investigate their intriguing properties, researchers have devoted great efforts to synthesize various t-TMDs by different methods. Generally, the stacking method and one-step chemical vapor deposition (CVD) method are the two major strategies adopted, which will be elaborated in the subsequent part. Apart from the reliable production, property characterization and examination are the other important research fields of t-TMDs. Unfortunately, there is no such review paper deliberating the synthesis and the properties of t-TMDs. This Review endeavors to provide an update-to-date overview of the recent progress in the synthesis of t-TMD bilayers and the study of the associated properties. The detailed synthesis methods are presented and discussed. The characterization techniques, including PL spectroscopy, Raman spectroscopy, and transmission electron microscopy (TEM), are also introduced. In addition, the intriguing physical characteristics of t-TMDs such as interlayer excitons and

correlated electronic phases are highlighted. Finally, the prospects for future research on t-TMDs are offered.

## 2. Synthesis of 2D t-TMDs

There are mainly two routes to produce t-TMD bilayers, which are the stacking method and the one-step CVD method, as shown in Figure 1b. The stacking method can be regarded as a two-step method as well, whereby the TMD monolayer is initially grown or exfoliated on a substrate, followed by transferring the monolayer onto another monolayer through a stacking or stamping process (route I). By doing so, the twist angle of the bilayers can be manipulated. Having said that, it is possible to use this route to create a heterogeneous bilayer that combines two distinct TMDs. The other method is relatively more straightforward. One-step CVD, as the name suggests, can grow twisted bilayers in a one-time CVD process as it does not require growing, transferring, and stacking of monolayers (route II). The main achievements in the preparation of t-TMDs are summarized in **Table 1**. The following parts will provide more discussions about the synthesis routes in a detailed manner as well as point out their respective pros and cons.

### 2.1. Stacking

The quality of the twisted bilayer largely relies on the monolayer obtained during the first stage of the procedure, which is used in

**Table 1.** Summary of the preparation of the t-TMD bilayers.

	Materials	Transfer method	Annealing conditions	Twist angle produced	Ref.
Stacking	MoS <sub>2</sub>	Dry transfer	400 °C in Ar atm for 3 h	$\theta = 17.7^\circ, 51.5^\circ, \text{ and } 84.7^\circ$	[32]
	MoSe <sub>2</sub>	Wet transfer	300 °C in Ar (95%)/H <sub>2</sub> (5%) at atm pressure for 2 h	$\theta$ ranging from 33.3° to 60.0°	[37]
	W-doped MoSe <sub>2</sub>	Wet transfer	300 °C in Ar (95%)/H <sub>2</sub> (5%) at atm pressure for 2 h	$\theta$ ranging from 40.8° to 60.0°	[37]
	WSe <sub>2</sub> /WS <sub>2</sub> heterostructure	Wet transfer	350 °C in Ar flow (90 sccm, 10 Torr) for 3 h	Eight different twist angles	[36]
	Materials	Precursors	Growth conditions	Twist angle produced	Ref.
One-step CVD	MoS <sub>2</sub>	20 mg MoO <sub>3</sub> , 7 mg S	Sit at 105 °C with 500 sccm N <sub>2</sub> for 1 h; ramp to 700 °C at 15 °C min <sup>-1</sup> and sit for 5–10 min with 10–15 sccm N <sub>2</sub> ; cool down naturally with 500 sccm N <sub>2</sub>	$\theta$ ranging from 0° to 60.0°	[34]
	MoSe <sub>2</sub>	MoO <sub>3</sub> , Se powder	$T_{\text{se}} = 300^\circ\text{C}$ , $T = 700^\circ\text{C}$ , 65 sccm Ar and 5 sccm H <sub>2</sub> , $t = 10$ min	$\theta = 7^\circ, 21^\circ, \text{ and } 25^\circ$	[33]
	WS <sub>2</sub>	WO <sub>3</sub> powder, 0.1 g S powder	200 sccm pure Ar for 30 min before heating; 20 sccm Ar for ramping to 1100 °C at the rate of 20 °C min <sup>-1</sup> ; growing for 20 min	$\theta = 0^\circ, 13^\circ, 30^\circ, 41^\circ, 60^\circ, \text{ and } 83^\circ$	[35]

the subsequent stacking process. Traditionally, ultrathin or monolayer TMDs can be produced by a chemical or mechanical exfoliation method. However, the procedure can be troublesome as it is difficult to maintain uniformity throughout the sample. Moreover, the flakes produced are generally small in size.<sup>[38]</sup> To address that, researchers have found that CVD is able to produce large-area domains as the experiment parameters in CVD can be finely controlled, thereby tuning the sample morphology. There have been many review articles describing the methodology of CVD to synthesize high-quality and large-area TMD monolayer.<sup>[39–43]</sup> The important roles played by various control parameters have been respectively discussed, such as reaction temperature, reaction time, ramp rate, and carrier gas flow rate, providing useful insights into the controllable CVD synthesis of 2D materials with desirable quality. With that being said, CVD experiment parameters play a vital role in determining the quality of the material. The same strategy is applied in the first step of the stacking method to produce t-TMDs. Apart from the CVD method, recent progress on the improvement of the exfoliation technique, i.e., the Au-assisted mechanical exfoliation method, has opened up more possibilities for constructing stacked t-TMCs. More than 40 types of single-crystalline monolayers have been obtained with the aforementioned exfoliation method, as reported by Huang et al.<sup>[44]</sup> When the monolayer is successfully grown or exfoliated on a substrate, it is then subjected to the subsequent transferring process. There have been many attempts to produce t-TMDs by manual transferring or stacking of the monolayers. The stacking process can generally be divided into two types, i.e., wet transfer and dry transfer.

Using the wet transfer method, Poretzky et al. obtained twisted MoSe<sub>2</sub> (t-MoSe<sub>2</sub>) bilayers with multiple stacking

orientations.<sup>[37]</sup> Briefly, the MoSe<sub>2</sub> monolayer was first grown on a SiO<sub>2</sub>/Si substrate using the CVD method. The chip was cut into two pieces, and one of them was spin coated with poly-methyl methacrylate (PMMA). Etching of the silicon substrate later took place by soaking the coated chip into a KOH solution, to obtain a freestanding PMMA/MoSe<sub>2</sub> film. The film was then rinsed in a beaker filled with deionized (DI) water to remove the KOH residue. Subsequently, the bilayer MoSe<sub>2</sub> was fabricated by stacking the rinsed film onto the second half of the chip with the originally grown monolayer MoSe<sub>2</sub>. Prior to the final annealing process, the stacked chip was soaked in an acetone solution to remove PMMA. The t-MoSe<sub>2</sub> bilayer sample was eventually obtained after annealing at 300 °C in an argon (Ar) and hydrogen (H<sub>2</sub>) environment at atmospheric pressure for 2 h. The prepared t-MoSe<sub>2</sub> possesses a broad range of twisted angles, from 33.2° to 60°, as shown in **Figure 2a**. The same procedure has also been applied to prepare twisted-bilayer W-doped MoSe<sub>2</sub> samples, with twisted angles ranging from 40.8° to 60° (**Figure 2b**). A similar transfer process has also been used by Huang et al. to prepare a t-MoS<sub>2</sub> bilayer.<sup>[32]</sup> Notably, both the top and bottom layer substrates were coated with PMMA. It was believed that the presence of PMMA in the bottom layer substrate may prevent the monolayer from being peeled off and degraded during assembly in water. However, it was hard to thoroughly remove the PMMA sandwiched in between by the conventional acetone method, degrading the quality of the as-prepared twisted-bilayer samples.

Apart from the twisted-bilayer homostructures, the wet transfer method has also been applied to assist the study of twisted-bilayer heterostructures. In 2016, Wang et al. reported the fabrication of WSe<sub>2</sub>/WS<sub>2</sub> bilayer heterostructures with various twist angles through artificially stacking CVD-grown WS<sub>2</sub> and

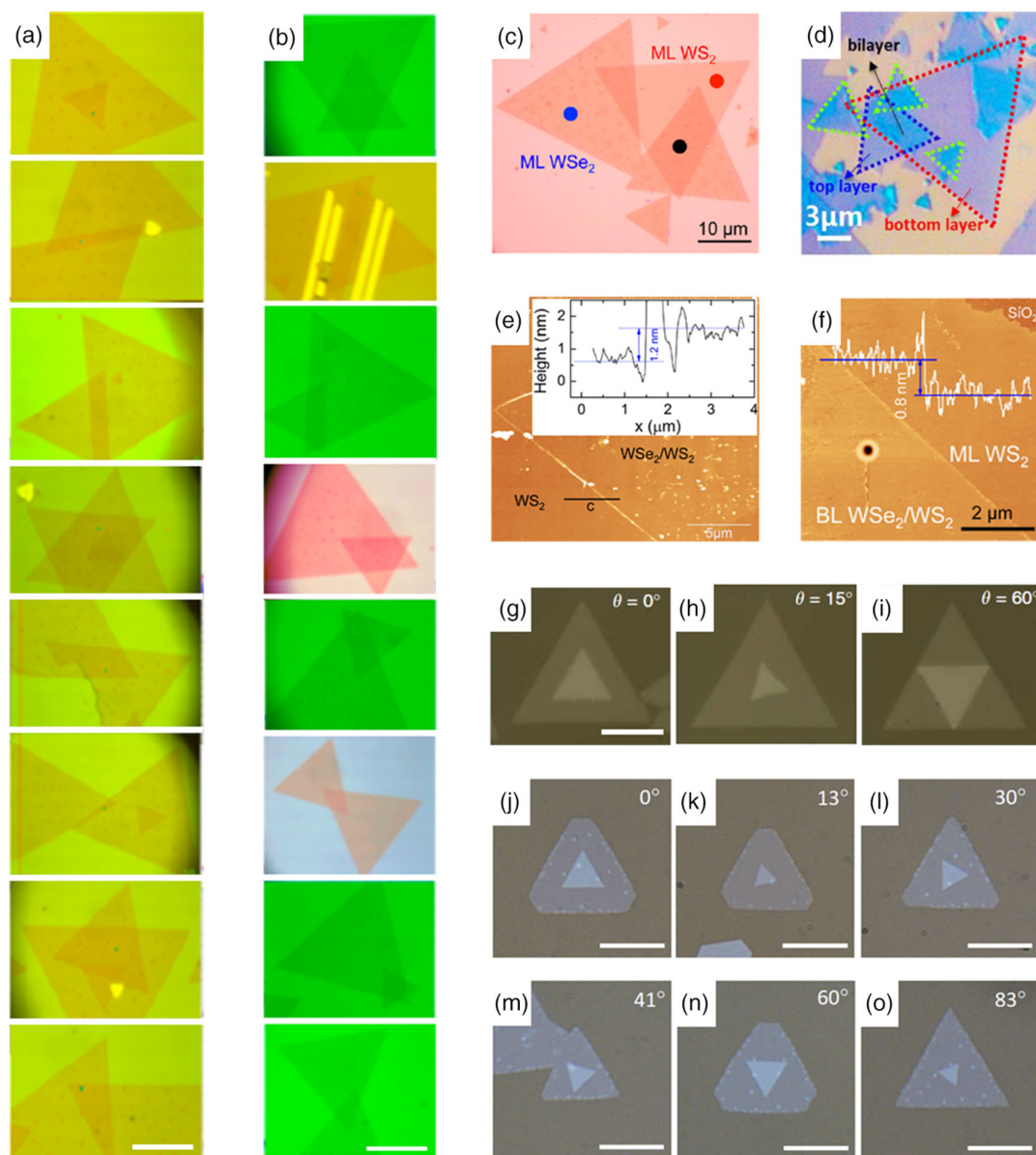


**Figure 2.** t-TMD bilayers obtained by two-step stacking or one-step CVD methods. a) OM images of bilayer MoSe<sub>2</sub> with the twist angle of 60.0°, 59.6°, 58.6°, 56.9°, 55.3°, 51.3°, 42.6°, and 33.2° (from top to bottom), respectively. b) OM images of bilayer W-doped MoSe<sub>2</sub> with the twist angle of 60.0°, 59.5°, 58.5°, 56.7°, 50.9°, 49.0°, 47.3°, and 40.8° (from top to bottom), respectively. Scale bar: 20 μm. a,b) Reproduced with permission.<sup>[37]</sup> Copyright 2016, American Chemical Society. c) OM image of WSe<sub>2</sub> monolayer, WS<sub>2</sub> monolayer, and the overlapping WSe<sub>2</sub>/WS<sub>2</sub> bilayer on a SiO<sub>2</sub>/Si substrate. d) OM image of the bilayer MoS<sub>2</sub> with the twist angle of 51.5°. The red and blue triangles show the area of interest, which refers to the bottom and top layers, respectively. c,d) Reproduced with permission.<sup>[32]</sup> Copyright 2014, American Chemical Society. e,f) AFM images of a twisted-bilayer WSe<sub>2</sub>/WS<sub>2</sub> and the corresponding sectional analysis before and after annealing, respectively. e,f) Reproduced with permission.<sup>[36]</sup> Copyright 2016, American Chemical Society. g–i) OM images of CVD-grown bilayer MoS<sub>2</sub> with twist angle 0°, 15°, and 60°, respectively. Scale bar: 10 μm. g–i) Reproduced with permission.<sup>[34]</sup> Copyright 2014, Nature Research. j–o) OM images of CVD-grown twisted WS<sub>2</sub> bilayers with twist angles 0°, 13°, 30°, 41°, 60°, and 83°, respectively. Scale bar: 10 μm. j–o) Reproduced with permission.<sup>[35]</sup> Copyright 2015, Wiley-VCH.

WSe<sub>2</sub> monolayers.<sup>[36]</sup> A typical constructed WS<sub>2</sub>/WSe<sub>2</sub> bilayer with a twist angle of 25.3° is shown in Figure 2c. As the twisted bilayer was heterogeneous with distinct materials, the two materials were grown separately on different substrates using different precursors and synthesis conditions. The rest of the procedures are rather similar, except that two additional

procedures are involved: 1) After the substrate with grown WS<sub>2</sub> was spin coated with PMMA, it was subjected to a curing process at 100 °C for 15 min to stabilize the monolayer flakes and 2) after the WSe<sub>2</sub>/WS<sub>2</sub> layers were stacked, the assembly went through a preheating step prior to the final annealing process to ensure the PMMA was thoroughly removed.

Instead of wet transfer, another research group has proposed the use of a dry transfer method to synthesize t-MoS<sub>2</sub> (Figure 1 and 2d).<sup>[32]</sup> The beginning of the dry transfer process was similar to the wet transfer method, from growing of monolayer MoS<sub>2</sub>, cutting into two pieces until obtaining the free-floating PMMA/MoS<sub>2</sub> top layer. Next, the PMMA/MoS<sub>2</sub> layer was put onto a polydimethylsiloxane (PDMS) elastomer that was attached to a glass slide, followed by baking at 130 °C to soften the PMMA. The assembly was then placed under a microscope with the MoS<sub>2</sub> layer facing down, and above the substrate with the bottom layer facing up. With the aid of a microscope, the top layer was adjusted and aligned with respect to the bottom layer. The glass slide was subsequently lowered down until touching the bottom layer, and the PDMS was slowly lifted, leaving the top layer in contact with the bottom layer. The stacked MoS<sub>2</sub> bilayer was eventually annealed at 400 °C in an Ar atmosphere for 3 h to strengthen the assembly. Notably, PMMA was not introduced between the top and bottom layers at all in the dry transfer process. Without interference from the foreign substance, the interlayer coupling between the two layers is therefore strong. Compared with the wet transfer method, removal of the PMMA residual in the dry transfer method was achieved only by annealing without the acetone-soaking process, which can help minimize the degradation and oxidation caused by the liquid. In addition, with the support of a glass slide and the aid of a microscope, the stacking process of the dry transfer method has higher controllability. Nevertheless, in the case of good sample coverage on the substrate, the wet transfer method should be an efficient method as t-TMDs with a broad range of twist angles can be obtained without involving the microscope alignment process.

Regardless of wet or dry transfer, proper annealing is of great importance to the interlayer coupling of the stacked-bilayer samples. It can help to remove adsorbates and polymer residues during the transferring process, as well as enhancing the vdW coupling between the top and bottom layers. Wang et al. particularly examined the atomic force microscopy (AFM) images of the fabricated twisted WSe<sub>2</sub>/WS<sub>2</sub> bilayers.<sup>[36]</sup> They found that the step height before and after annealing was ≈1.2 and ≈0.8 nm, respectively, indicating the establishment of vdW coupling between two decoupled layers during the annealing process, as shown in Figure 2e,f. Moreover, without annealing, the sample quality is compromised, which affects relevant characterization results. For example, no low-frequency (LF) Raman lines of as-prepared twisted-bilayer samples can be observed before annealing.<sup>[37]</sup>

In addition to the commonly used etching-assisted wet/dry transfer method, some dry peel-off methods have also been developed to fulfill the transferring purpose in recent years. For instance, Ma et al. reported a capillary-force-assisted clean stamp technique to pick up and transfer 2D materials.<sup>[45]</sup> A thin layer of vapor (e.g., water) is the key to enhance the adhesion energy between 2D materials and PDMS, thereby facilitating the pick-up process. Once the vapor evaporates, the adhesion energy decreases, and 2D materials can be easily released on to the targeted substrate. This method holds great promise for the on-chip transfer of materials. Another peel-off method was developed by Tao et al. in 2018.<sup>[46]</sup> A water-soluble polyvinyl alcohol (PVA) thin film was used for sample pickup, and could then be easily removed by a floating dissolution process. These novel

transfer methods provide new opportunities for the preparation of large-area high-quality t-TMDs.

## 2.2. One-Step CVD

CVD is one of the most important and popular techniques to produce high-quality inorganic nanomaterials. To date, numerous 2D TMDs, as well as their heterostructures, have been constructed by the increasingly matured CVD methods.<sup>[19,25,39–43]</sup> It is thus a promising method to obtain t-TMD bilayers without the involvement of sample transfer.

Using MoO<sub>3</sub> and S powder as precursors, Liu and colleagues demonstrated the growth of bilayer MoS<sub>2</sub> on mica, fused silica as well as a SiO<sub>2</sub>/Si substrate through ambient pressure chemical vapor deposition (APCVD).<sup>[34]</sup> Unlike the conventionally used Ar gas, ultrahigh-purity nitrogen (N<sub>2</sub>) gas was used as the carrier gas to deliver the S particles to the center of the furnace to react with MoO<sub>3</sub>. It is worth noting that the core idea of tuning the CVD parameter is to reduce the nucleation rate during the initial growth stage to render the vertical layer-by-layer growth mode more preferable. It was observed that the ratio of MoS<sub>2</sub> bilayer to monolayer is positively correlated with the growth time. At the reaction temperature of 700 °C, bilayers with yield up to 30% was achieved after 10 min growth. Optical images of typical grown t-MoS<sub>2</sub> bilayers with angles of 0°, 15°, and 60° are shown in Figure 2g–i. Direct CVD synthesis of t-MoS<sub>2</sub> was also achieved by Lin et al. in 2018.<sup>[47]</sup>

Alternatively, Bachmatiuk and co-workers also reported the CVD fabrication of t-MoSe<sub>2</sub> bilayer on SiO<sub>x</sub> substrate with a purpose-built horizontal-furnace reactor.<sup>[33]</sup> In addition to Ar gas, H<sub>2</sub> gas was also introduced into the chamber when the reaction was taking place. H<sub>2</sub> plays an important role in the experiment because it acts as a reducing agent to reduce the precursors, thereby promoting the chemical reaction.<sup>[48]</sup> Both a monolayer and a t-MoSe<sub>2</sub> bilayer were yielded using this route.

In another report by Zheng et al., the one-step CVD method was also used to synthesize a twisted WS<sub>2</sub> (t-WS<sub>2</sub>) bilayer on quartz plates with twist angles of 0°, 13°, 30°, 41°, 60°, and 83°, as shown in Figure 2j–o.<sup>[35]</sup> The procedures are similar to the aforementioned ones, except that a piece of magnet was applied to push the sulfur precursor to the edge of the furnace when the designated reaction temperature was reached so that the S powder melted and supplied S vapor to the reaction center. Moreover, the authors found that temperature and nucleation play vital roles in material synthesis. Bilayer t-WS<sub>2</sub> could only be observed at the high growth temperature of 1100 °C. At a lower growth temperature of 850 °C, only conventional AA and AB stacking bilayers could be obtained. It was speculated that at a high temperature, the top layer tends to grow along with its original nucleus orientation and overcome the angular mismatch with the bottom layer.

Considering the predominant effect of the twist angle on the properties of TMDs, substantial research effort has been devoted by the community to achieve the precise control of the twist angle. Up to now, it is still a great challenge to control the twist angle of CVD-grown bilayer TMDs due to the complex CVD environment. Nevertheless, with the intensive study, more and more

useful information has been unveiled, paving the way for controllable synthesis in the future. For example, Mandyam et al. studied the twist angle distribution of around 100 CVD-grown bilayer WSe<sub>2</sub> flakes.<sup>[49]</sup> They found that the majority showed a twist angle of 0°/60° (≈84%), whereas the rest showed the twist angles of 30° (12%) and 15° (4%). This distribution of twist angles agrees well with the calculated stacking energy density, with the 0/60° showing the lowest values, followed by 30° and 15° twisted structures. Zhang et al. have further investigated the temperature effect on the thermodynamically stable 0°/60° configurations and observed that AA stacking (0°) of bilayer MoS<sub>2</sub> is favorable at a lower temperature (i.e., 750 °C), whereas AB stacking (60°) is generally obtained at a higher temperature (i.e. 800 °C).<sup>[4]</sup> Very recently, the direct growth of continuously twisted superstructures of WS<sub>2</sub> and WSe<sub>2</sub> has been reported by Zhao et al. through the introduction of non-Euclidean surfaces to the growth process. This work contributes greatly to the precise control of twist angles and will be discussed in detail in the next section.<sup>[50]</sup>

### 2.3. Discussion

Both stacking and one-step CVD methods have demonstrated their ability to produce t-TMDs, and each group of researchers has slightly different methods. For the stacking method, the procedure is rather tedious as it involves a transfer step, which is a bit challenging and time-consuming. However, one benefit of this stacking method is that it is easier to produce twisted-heterostructure bilayers because the top and bottom layers are initially separated. In addition, with the help of a microscope, the stacking process can be fairly controlled to achieve desirable twist angles. It is noteworthy that the final annealing process plays a significant role in the preparation of t-TMDs because it directly affects the coupling relationship between the two layers, by removing adsorbates and PMMA residues during the transferring process. Various annealing conditions have been explored by different groups to eliminate the PMMA residue. For example, some researchers involved a PMMA curing step prior to the etching process, or a prebaking step before the final annealing process, whereas other experimenters did not.

Compared with the stacking method, the one-step CVD method is relatively faster as the sample transferring and stamping processes are no longer required. The CVD methods to produce monolayer, bilayer, or even multilayer materials are rather similar. It is the control parameters that depict the final product. Therefore, synthesis parameters used for synthesizing t-TMD bilayers have to be extremely precise. In general, a relatively high reaction temperature is required because randomly twisted bilayers are thermodynamically unfavorable, and the interlayer bonding requires higher activation energy to form. In addition, the reaction time is also critical to promote the formation of bilayer TMDs. For instance, in the case of CVD-grown t-MoS<sub>2</sub> bilayers, the ratio of MoS<sub>2</sub> bilayer to monolayer was found to increase with the reaction time.<sup>[34]</sup>

Although the two methods discussed previously can meet most research needs of t-TMDs, it is still a bit challenging to produce a clean interface and controlled twist angles (especially a small twist angle) simultaneously. Thus, when performing

certain experiments where such controllability is very much demanded, a more delicate preparation method is required. When Cao et al. dig into the exotic physical properties of (TBG, the “magic” angle of ≈1.1° needs to be accurately achieved.<sup>[13,14,51]</sup> The technique adopted was “tear and stack”, which enables subdegree control of the twist angle.<sup>[52,53]</sup> Its schematic is displayed in Figure 3a. Poly (bisphenol-A carbonate) (PC)/PDMS stacked on a glass slide is first used to pick to a piece of hexagonal boron nitride (h-BN) at 90 °C. The h-BN is then brought into contact with one-half of a graphene flake. When lifting the glass, the graphene tears into two halves, where one half is bonded to h-BN due to vdW interaction, and the other is held to the substrate. Next, the substrate is rotated by the desired angle. Eventually, the TBG is obtained after lowering down the glass to pick up the remaining graphene.

A typical TBG-based device structure is shown in Figure 3b. The enlarged view clearly shows two graphene layers twisted relative to each other. Unconventional superconductivity (Figure 3c) and correlated insulator states at half filling (Figure 3d) were observed in “magic” angle TBG, indicating the great importance of the controllable synthesis of clean and small-twist-angle bilayers. In addition to the magic TBG, the “tear-and-stack” technique has also been successfully applied to obtain WSe<sub>2</sub> bilayers with twist angles ranging from 0° to 17°.<sup>[54]</sup> Especially, a small twist angle of around 0° has been attained (Figure 3e). Very recently, MoSe<sub>2</sub>/MoSe<sub>2</sub> bilayers with near 0° twist angle have been prepared by Sung et al. with this method as well (Figure 3f), which demonstrate broken mirror/inversion symmetry.<sup>[29]</sup> The effect of crystal symmetry on TMD excitons was investigated and revealed. This twist angle control should be generalizable to more 2D systems, which may exhibit more intriguing physics behaviors.

Apart from the “tear-and-stack” technique, another method with atomic precision was reported by Gao et al. in 2019.<sup>[55]</sup> A scanning tunneling microscope (STM) tip was adopted to manipulate the folding and unfolding of graphene nanoislands, as shown in Figure 3g. TBG with controllably tunable twist angles was successfully prepared. The obtained twist angles are analyzed and summarized in Figure 3h. This STM origami method holds great promise for the construction of atomically precise nanostructures with quantum properties and shall be extended to the preparation of t-TMDs.

It is worth mentioning that the latest work reported by Zhao et al. provides new insights into the fabrication of t-TMDs.<sup>[50]</sup> Continuously twisted superstructures of TMDs including WS<sub>2</sub> and WSe<sub>2</sub> can be obtained by their proposed method, which is shown in Figure 3i. The key idea is to introduce non-Euclidean surfaces into the CVD growth process, which can be achieved by drop casting nanoparticles as protrusions on flat Si/SiO<sub>2</sub> substrates. The combined screw-dislocation spirals and non-Euclidean surfaces together result in supertwisted spiral TMDs, as shown in Figure 3j–m.

## 3. Characterization of 2D t-TMDs

The properties of t-TMDs can be characterized by various kinds of instruments, and PL and Raman spectroscopy are the two most commonly used characterization tools. PL spectroscopy

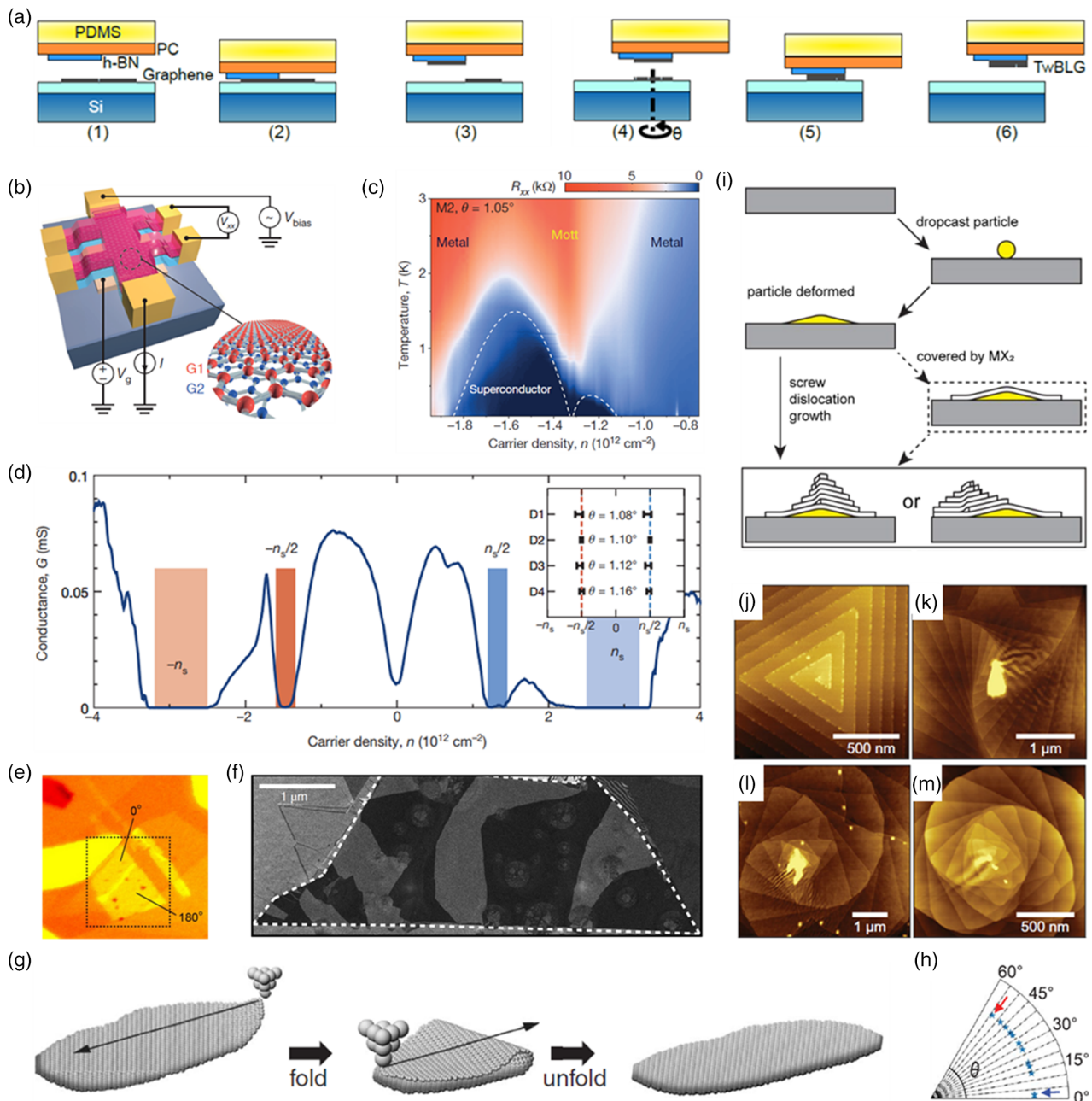


**Figure 3.** The emergence of more sophisticated techniques for controllably preparing bilayers with small twisted angles. a) Schematic illustration of the “tear-and-stack” technique. Reproduced with permission.<sup>[45]</sup> Copyright 2017, American Chemical Society. b) Schematic of a typical TBG-based device. c) Four-probe resistance ( $R_{xx}$ ) of the “magic” angle TBG-based device measured at a narrow carrier density range versus temperature, indicating the unconventional superconductivity. b,c) Reproduced with permission.<sup>[13]</sup> Copyright 2018, Springer Nature. d) The conductance ( $G$ ) of the “magic” angle TBG-based device measured at  $T = 0.3$  K, revealing the half-filling insulating states. Reproduced with permission.<sup>[14]</sup> Copyright 2018, Springer Nature. e) Optical image of the t-WSe $_2$  bilayers with near  $0^\circ$  twist angle, obtained by the “tear-and-stack” technique. Reproduced with permission.<sup>[54]</sup> Copyright 2020, American Physical Society. f) Dark-field TEM image of a MoSe $_2$ /MoSe $_2$  bilayer with near  $0^\circ$  twist angle. The dark and gray regions correspond to the alternating domains with rhombohedral stacking symmetry. Reproduced with permission.<sup>[29]</sup> Copyright 2020, Springer Nature. g) Schematic graphic of the STM origami process of folding and unfolding graphene nanoislands. h) Summary of the twist angles obtained. g,h) Reproduced with permission.<sup>[55]</sup> Copyright 2020, American Association for the Advancement of Science. i) Schematic illustration of the formation process of supertwisted spirals of layered materials. j) AFM image of aligned WS $_2$  spirals grown on flat SiO $_2$ /Si substrate. k–m) AFM images of supertwisted WS $_2$  spirals grown around the dropcasted particles on SiO $_2$ /Si substrate. i–m) Reproduced with permission.<sup>[50]</sup> Copyright 2020, American Association for the Advancement of Science.

can be used to study the optical properties of the material after absorption of photons from a graph of intensity versus wavelength because the interlayer coupling between the bilayers changes the band structure and therefore alters the PL emission. Raman spectroscopy makes use of the molecule mechanical vibration to provide information on the change of phonon vibrations.<sup>[56]</sup> Apart from them, optical microscopy (OM), AFM, TEM, density functional theory (DFT) calculations, etc., have also been used to assist in the identification of twisted bilayers.

### 3.1. PL Spectroscopy

The interlayer coupling can modify the electronic band structure of TMD bilayers significantly, and PL spectroscopy is a useful tool to unveil such changes. Zheng et al. have studied the PL spectra of t-WS<sub>2</sub> bilayers with different twist angles, as shown in Figure 4a.<sup>[35]</sup> It has been observed that randomly twisted WS<sub>2</sub> (13°, 30°, 41°, and 83°) has much higher PL intensity than the 0° (AA stacking) and 60° (AB stacking) twisted ones. Apart

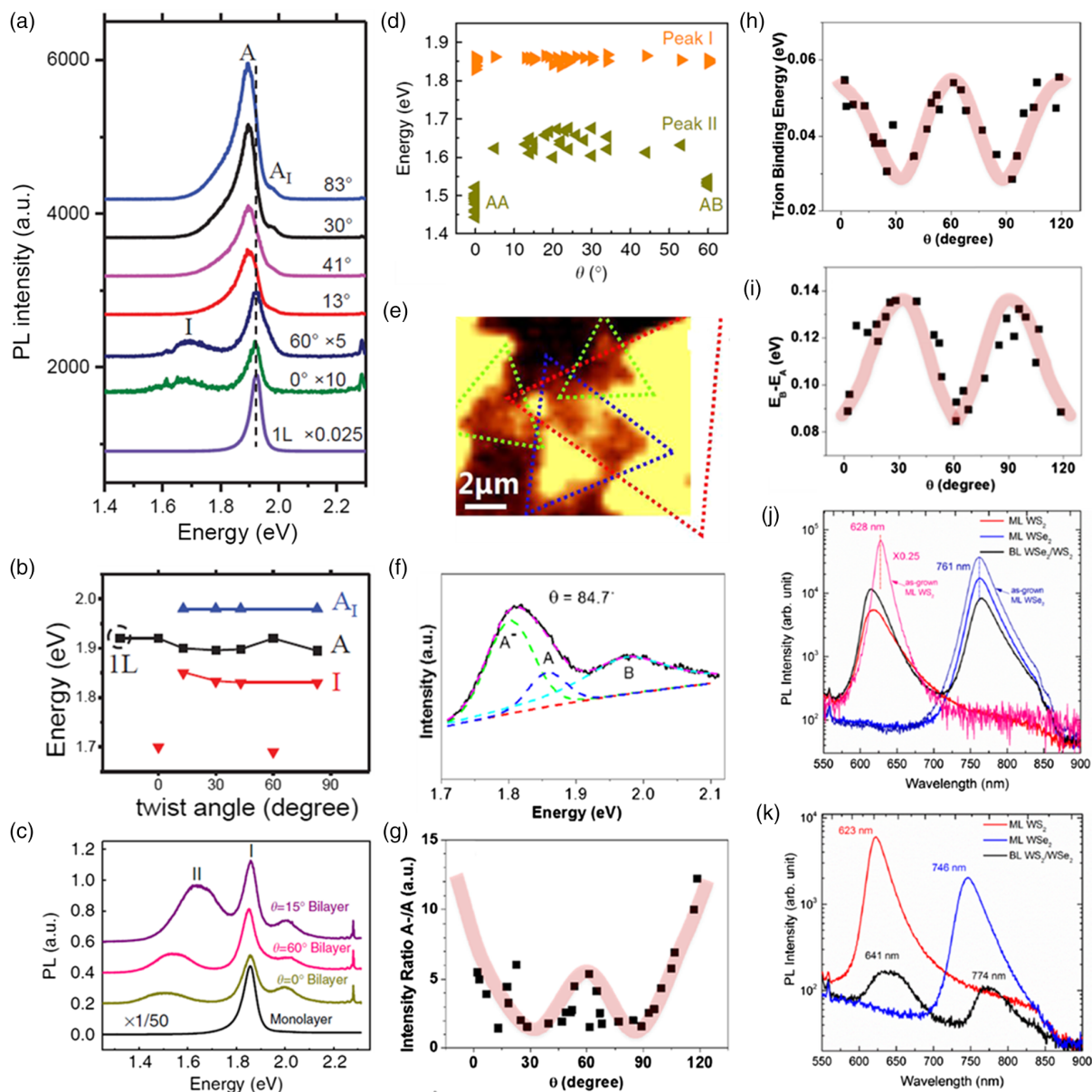


**Figure 4.** PL study of the electronic coupling evolution in t-TMD bilayers. a) PL spectra of monolayer and bilayer WS<sub>2</sub> with the twist angle of 0°, 13°, 30°, 41°, 60°, and 83°. b) Plot of PL peaks' positions of the curves in (a) obtained by Lorentz fitting with respect to the twist angle. a,b) Reproduced with permission.<sup>[35]</sup> Copyright 2015, Wiley-VCH. c) PL spectra of monolayer and bilayer MoS<sub>2</sub> with the twist angle of 0°, 15°, and 60°. d) Dependence of PL peak energies of 44 MoS<sub>2</sub> bilayers with respect to different twist angles. c,d) Reproduced with permission.<sup>[34]</sup> Copyright 2014, Nature Research. e) Mapping of the PL integrated intensity of a twisted-bilayer MoS<sub>2</sub> flake obtained by stacking. f) PL spectrum of the MoS<sub>2</sub> bilayer with the twist angle of 84.7°. g–i) Twist angle dependence of the A<sup>-</sup> trion to the A exciton PL intensity ratio (g), trion binding energy (h), and difference of PL peak energy between B and A excitons ( $E_B - E_A$ ) (i). e–i) Reproduced with permission.<sup>[32]</sup> Copyright 2014, American Chemical Society. j,k) PL spectra of twisted bilayer WSe<sub>2</sub>/WS<sub>2</sub> obtained by stacking on SiO<sub>2</sub>/Si substrate before and after annealing. j–k) Reproduced with permission.<sup>[36]</sup> Copyright 2016, American Chemical Society.



from that, the  $0^\circ$  and  $60^\circ$  stacked bilayers show two dominating peaks, i.e., peak A and peak I, corresponding to direct and indirect transitions, respectively. This is consistent with previous reports that t-WS<sub>2</sub> with  $0^\circ$  and  $60^\circ$  twist angles are indirect-bandgap materials.<sup>[57,58]</sup> In contrast, there is no indirect transition peak I in the spectra of randomly twisted bilayers. However, it was found that the spectra of randomly twisted bilayers have a minor peak A<sub>1</sub>, which is believed to be the interlayer excitonic transition. To better illustrate the changes of PL spectra, a plot of PL peaks' positions obtained by Lorentz fitting with respect to the twist angle is shown in Figure 4b. The indirect-bandgap energy (peak I) is an indicator of the interlayer electronic coupling strength: the lower the indirect bandgap energy, the stronger the coupling strength.<sup>[34]</sup> Ab initio calculation has later been applied to verify that the weakened interlayer coupling between randomly twisted bilayers results from the enlarged interlayer distance.

A similar twist-angle-dependent trend has also been observed in CVD-grown MoS<sub>2</sub> bilayers by Liu et al.<sup>[34]</sup> Figure 4c displays the PL spectra of monolayer as well as bilayer MoS<sub>2</sub> with twist angles of  $0^\circ$ ,  $15^\circ$ , and  $60^\circ$ . For all the bilayers, the PL intensity decreases significantly compared to the intensity of monolayer PL. In addition, they found that a minor peak II with lower energy resulting from an indirect bandgap appeared in the twisted bilayer PL spectra. To further clarify the interlayer coupling between the bilayers, they did the same measurement for plenty of samples with various twist angles and then plotted the transition energies of peak I and II (Figure 4d). As can be seen, peak I shows consistent energy for all the different twist angles. However, for peak II, it was observed that the  $0^\circ$  twisted-bilayer MoS<sub>2</sub> and  $60^\circ$  twisted-bilayer MoS<sub>2</sub> have the lowest energy among the rest of the randomly twisted bilayers. Surprisingly, the trend is the same as that in the aforementioned Figure 4b, whereby the respective minor peaks for both materials have the lowest energy for the  $0^\circ$  and  $60^\circ$  stacked bilayers. This can also be explained by the stacking configuration of the bilayers. Bilayers with  $0^\circ$  and  $60^\circ$  angles have the most symmetric configuration; therefore, they are more stable. As a result,  $0^\circ$  and  $60^\circ$  twisted bilayers have the smallest indirect bandgap and the strongest interlayer coupling between the layers.

The PL spectra of a t-MoS<sub>2</sub> bilayer obtained by the stacking method have also been studied.<sup>[32]</sup> Similarly to CVD-grown MoS<sub>2</sub> bilayers, the t-MoS<sub>2</sub> bilayer has much lower PL intensity when compared to the monolayer, as indicated by the PL mapping result shown in Figure 4e. Moreover, it was found that the PL profile of bilayers varies with different twist angles. Figure 4f provides the typical PL spectrum of a t-MoS<sub>2</sub> bilayer with a twist angle of  $84.7^\circ$ . As shown in Figure 4g, the PL intensity ratio of the A<sup>-</sup> trion to the A exciton demonstrates an oscillatory behavior as a function of the twist angle. The curve is approximately symmetrical with respect to the twist angle of  $60^\circ$ , which is consistent with the symmetry of the D<sub>3h</sub> crystal structure of the monolayer MoS<sub>2</sub>. A similar oscillatory and periodic trend was also observed in the PL emission energy difference between the A and A<sup>-</sup> peaks, which indicates the binding energy of the trions (Figure 4h). Moreover, the difference between the PL peak energy of B and A excitons,  $E_B - E_A$ , exhibits similar but opposite periodic and oscillatory behavior, as shown in Figure 4i.  $E_B - E_A$  is inversely correlated to the interlayer coupling. When  $\theta = 0^\circ$  and  $60^\circ$ , the interlayer coupling is the strongest, whereas

$E_B - E_A$  reaches the minimum. Again, changes shown in the aforementioned curves suggest the variations of the interlayer coupling of MoS<sub>2</sub> bilayers with different twist angles.

Last but not least, Wang et al. adopted PL spectroscopy to study the electronic interlayer coupling evolution in the twisted heterostructure bilayers, i.e., WSe<sub>2</sub>/WS<sub>2</sub>.<sup>[36]</sup> In their work, they particularly examined the PL spectra of the twisted bilayers before and after annealing to study the effect of annealing on the PL emission (Figure 4j,k). It was found that after annealing, the PL intensity of WS<sub>2</sub> and WSe<sub>2</sub> significantly reduced by a factor of 37 and 18 in the heterojunction area, respectively, which is strong evidence suggesting the formation of interlayer coupling between two layers.

### 3.2. Raman Spectroscopy

Raman spectroscopy is one of the most useful techniques for studying the evolution of mechanical couplings in TMD bilayers because phonon vibrations in 2D TMDs are very sensitive to interlayer coupling.<sup>[59]</sup> In the study reported by Huang et al., Raman spectroscopy was adopted to study the properties of a t-MoS<sub>2</sub> bilayer obtained by the stacking method, with the twist angles of  $17.72^\circ$ ,  $51.5^\circ$ , and  $84.7^\circ$ .<sup>[32]</sup> The corresponding Raman spectra are shown in Figure 5a. Two prominent peaks can be identified in the range  $360\text{--}440\text{ cm}^{-1}$ , corresponding to the in-plane E<sub>2g</sub> and out-of-plane A<sub>1g</sub> phonon modes, respectively. However, no obvious angle dependence of the Raman signal can be observed in this work. Later, Liu and colleagues reported a more comprehensive Raman study of CVD-grown MoS<sub>2</sub> with various twist angles. They first studied the Raman spectra of monolayer and bilayer MoS<sub>2</sub> with twist angles of  $0^\circ$ ,  $15^\circ$ , and  $60^\circ$  (Figure 5b). They found that the E<sub>2g</sub> peaks of all the bilayers exhibit a constant redshift, whereas the A<sub>1g</sub> peak shows a twist-angle-dependent blueshift. Therefore, the separation between two peaks ( $\omega_A - \omega_E$ ) serves as an effective indicator of the mechanical interlayer coupling: the larger the separation, the stronger the mechanical coupling. To further reveal the twist angle dependence, Raman spectra of 44 MoS<sub>2</sub> bilayers with different twist angles were collected and analyzed, whose results are plotted in Figure 5c. It can be clearly identified that the AA or AB stacked bilayer possesses the strongest coupling, which agrees well with the result revealed by PL spectroscopy. Moreover, bilayers with other random twist angles possess weaker but constant coupling, consistent with the result obtained by Huang et al. that bilayer MoS<sub>2</sub> with the twist angle of  $17.72^\circ$ ,  $51.5^\circ$ , and  $84.7^\circ$  possess rather similar Raman spectra.

Apart from t-MoS<sub>2</sub>, Raman spectroscopy has also been applied to investigate the interlayer coupling of t-WS<sub>2</sub> bilayers.<sup>[35]</sup> Raman spectra of the WS<sub>2</sub> bilayers with random twist angles ranging from  $0^\circ$  to  $83^\circ$  are shown in Figure 5d. As expected, some characteristic differences indicate different phonon vibrations in the bilayers arising from the interlayer coupling effect. For example, the longitudinal acoustic phonon (2LA) peaks of the randomly twisted bilayer WS<sub>2</sub> have shifted to a higher wavenumber compared to the highly symmetrically configured  $0^\circ$  and  $60^\circ$  bilayers. Moreover, their A<sub>1g</sub> peaks are generally redshifted and broadened, suggesting the weaker interlayer mechanical coupling of randomly twisted bilayer WS<sub>2</sub> than the more stable AA or AB

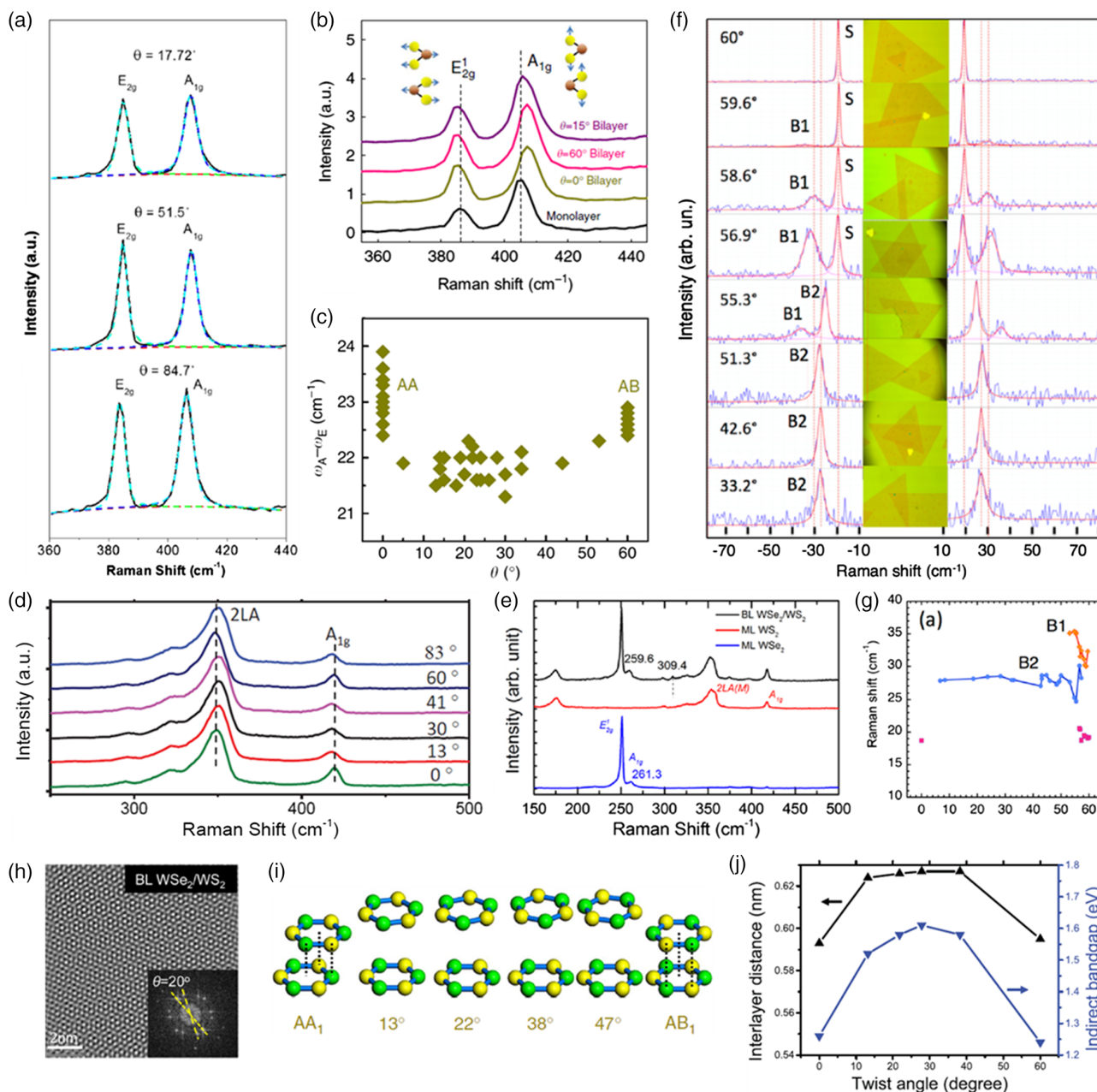


**Figure 5.** Raman and other characterizations of t-TMD bilayers. a) Raman spectra of stacked bilayer MoS<sub>2</sub> with the twist angle of 17.72°, 51.5°, and 84.7°. b) Raman spectra of CVD-grown monolayer and bilayer MoS<sub>2</sub> with the twist angle of 0°, 15°, and 60°. c) Plot of the Raman peak separation between the A<sub>1g</sub> and E<sub>2g</sub> modes ( $\omega_{A_1g} - \omega_{E_{2g}}$ ) versus the twist angles. d) Raman spectra of bilayer WS<sub>2</sub> with the twist angle of 0°, 13°, 30°, 41°, 60°, and 83°. e) Raman spectra of twisted bilayer WSe<sub>2</sub>/WS<sub>2</sub> obtained by stacking on a sapphire substrate. f) Stokes and anti-Stokes Raman spectra of bilayer MoSe<sub>2</sub> with twist angle ranging from 33.2° to 60°. g) Plot of the twist-angle-dependent Raman shifts of the shear and two breathing modes of stacked bilayer MoSe<sub>2</sub>. h) FFT-filtered TEM image of bilayer WSe<sub>2</sub>/WS<sub>2</sub> and corresponding FFT pattern. i) Schematics of bilayer MoS<sub>2</sub> with different twisted stackings. Mo and S atoms are shown in green and yellow balls, respectively. j) Plot of calculated interlayer distance and indirect bandgap of bilayer WS<sub>2</sub> with respect to twist angles. a) Reproduced with permission.<sup>[32]</sup> Copyright 2014, American Chemical Society. b,c,i) Reproduced with permission.<sup>[34]</sup> Copyright 2014, Nature Research. d,j) Reproduced with permission.<sup>[35]</sup> Copyright 2015, Wiley-VCH. e,h) Reproduced with permission.<sup>[36]</sup> Copyright 2016, American Chemical Society. f,g) Reproduced with permission.<sup>[37]</sup> Copyright 2016, American Chemical Society.

stacked bilayers. This finding is in good agreement with the result observed from MoS<sub>2</sub>.

In addition to bilayers made of the same material, Raman spectroscopy can also be used to reveal the interlayer coupling

of bilayer heterostructures. For example, Wang et al. studied the Raman spectra of a WSe<sub>2</sub>/WS<sub>2</sub> heterostructure obtained by the stacking method, as shown in Figure 5e.<sup>[36]</sup> They noted that the A<sub>1g</sub> peak of WSe<sub>2</sub> in the bilayer spectra was redshifted

with respect to its monolayer spectra. As  $\text{WSe}_2$  generally redshifts as the number of layers increase, the presence of interlayer coupling between  $\text{WS}_2$  and  $\text{WSe}_2$  could thus be confirmed. Moreover, a new peak at  $309.4\text{ cm}^{-1}$  appeared, which corresponds to a layer-number-sensitive vibrational mode of  $\text{WS}_2$ . This again shows the interlayer coupling effect between two stacked layers.

An alternate effort has been devoted by Puzetzy et al. to utilize LF Raman spectroscopy to determine the interlayer coupling between t- $\text{MoSe}_2$  bilayers.<sup>[37]</sup> Compared with the conventional Raman approach, LF Raman spectroscopy is more sensitive to probing vdW interlayer coupling as it can detect the in-plane shear and out-of-plane breathing vibrations of the entire 2D layer moving as a whole unit.<sup>[37,56,60,61]</sup> It has already been successfully applied to study the effect of interlayer coupling on twisted multilayer graphene.<sup>[62,63]</sup> Figure 5f shows the Stokes and anti-Stokes LF Raman spectra of t- $\text{MoSe}_2$  bilayers with twist angles ranging from  $33.2^\circ$  to  $60^\circ$ . Notably, the acquired LF Raman spectra possess a highly sensitive response to the interlayer coupling, and even a slight deviation of the twist angle may result in very different Raman spectra. For instance, a slight twist angle has caused the breathing mode  $B_1$  to appear in the spectrum of  $59.6^\circ$  but not in the one of  $60^\circ$ . The intensity of the  $B_1$  peak becomes much more pronounced as the twist angle further decreases to  $56.9^\circ$ . Another interesting feature is that the shear mode peak S quickly disappears when the twist angle decreases to  $55.3^\circ$ . This could be attributed to the reduction of the in-plane restoring force as stacking becomes unaligned with mismatched periodicity. Apart from that, a new breathing peak B2 shows up when the twist angle decreases to  $55.3^\circ$ , corresponding to the mismatched alignments. For better visualization, the Raman shifts of the shear and breathing modes with respect to the twist angles are summarized and shown in Figure 5g. The same set of samples has also been investigated using high-frequency (HF) Raman spectroscopy, and it was found that the spectra have much fewer variations of frequency and intensity with the twist angle.

Almost at the same time, Huang et al. reported the LF Raman study of t- $\text{MoS}_2$  bilayers.<sup>[64]</sup> Similar findings have been demonstrated that the LF modes are much more responsive to the interlayer stacking and coupling in contrast to the HF Raman modes. Especially, when the twist angle is near  $0^\circ$  and  $60^\circ$ , the frequency and intensity variation of LF modes can reach  $8\text{ cm}^{-1}$  and five times, respectively. Therefore, it can be summarized that LF Raman spectroscopy is sometimes more effective in studying interlayer stacking and coupling as it can provide more detailed and comprehensive characterization.

### 3.3. Other Techniques

In addition to PL and Raman spectroscopy, OM, AFM, TEM, and DFT calculations have also been applied to identify and study the t-TMD bilayers. As shown in Figure 2, most twisted samples can be observed from the OM images directly due to the color contrast. AFM is a very high-resolution type of scanning probe microscopy (SPM), which can probe the boundary between the monolayer and bilayer. On top of that, the corresponding height profile can also be used to investigate the formation of

interlayer coupling, as discussed earlier (Figure 2e,f). TEM is another effective tool to study the structure of t-TMDs on a microscopic scale. For example, Figure 5h shows a fast Fourier transform (FFT)-filtered TEM image of bilayer  $\text{WSe}_2/\text{WS}_2$ .<sup>[36]</sup> Moiré fringes can be clearly observed, resulted from the overlaying of lattice-mismatched or rotated 2D heterostructures.<sup>[65]</sup> The twist angle of  $20^\circ$  can be determined by measuring the two hexagonal reciprocal lattices in the image.

To understand the origin of changes in properties, various research groups have performed DFT calculations to study the coupling evolution of t-TMD bilayers. It has been found that the interlayer distance of t- $\text{MoS}_2$  bilayers has a strong variation with respect to various twist angles, as shown in Figure 5i.<sup>[34]</sup> The most stable AA- and AB-stacked  $\text{MoS}_2$  possesses the smallest interlayer separation of  $\approx 0.61\text{ nm}$ , and the separation of the four twisted  $\text{MoS}_2$  is  $\approx 0.65\text{ nm}$ . This can be understood physically through repulsive steric effects. For the twisted-bilayer  $\text{MoS}_2$ , the S atoms of the top layer are located near the S atoms of the bottom layer. Therefore, the resulting repulsion between adjacent S atoms leads to a larger interlayer distance. On the contrary, in the energetically favorable AA and AB stackings, the S atoms of the top layer correspond to the trigonal vacancies of the S atoms of the bottom layer in a staggered manner, thereby reducing the repulsion and minimizing the interlayer distance. A similar result has also been reported on the CVD-grown t- $\text{WS}_2$  bilayers (Figure 5j).<sup>[35]</sup> In addition, it has been found that the twisted bilayer has a larger indirect bandgap than the one with AA or AB stacking. The larger interlayer distance and indirect bandgap together indicate the weaker interlayer couplings in twisted bilayers.

## 4. Physical Properties of 2D t-TMDs

Moiré superlattices can be formed by vertically stacking two layers of materials with different lattice constants and/or with a twist angle, as shown in Figure 5h. The corresponding moiré potential landscapes enable the emergence of exotic phenomena with a variety of building blocks, such as fractal quantum Hall effect and tunable Mott insulators in graphene/ $\text{BN}$  moiré superlattices<sup>[11,12,14,66,67]</sup> and unconventional superconductivity in TBG.<sup>[13]</sup> Recent studies have not only given an insight into the relationship between twist angles and the optoelectronic performance of heterojunctions, but also established t-TMDs as a promising platform to investigate interlayer excitons and correlated physics.<sup>[30,31,54,68–70]</sup>

### 4.1. Identification of Interlayer Excitons

Theory predicts that remarkable effects on optical excitations could be resulted from the moiré potential in 2D valley semiconductors with the Coulomb bounded electrons and holes in different monolayers.<sup>[28,71,72]</sup> These interlayer excitons exhibit many appealing properties, such as valley-contrasting physics,<sup>[28,71–78]</sup> long population and valley lifetimes,<sup>[73,79–81]</sup> high electrical tunability,<sup>[73,77,79,82]</sup> and strong many-body correlations.<sup>[73,79,80]</sup> However, the signatures of these interlayer excitons had not been detected through experiments until Seyler et al. reported evidence of moiré-trapped interlayer valley excitons in  $\text{MoSe}_2/\text{WSe}_2$

heterobilayers.<sup>[69]</sup> They observed PL peaks about two orders narrower than free interlayer excitons near the same energy at low temperatures (**Figure 6a**) indicating the presence of trapped excitons. The trapped interlayer excitons show strong circular valley polarization, which has the same helicity for a given twist angle, suggesting that the trapping potential is a result of the moiré landscape preserving the threefold rotational symmetry.

Jin et al. also provided insight into the emergent moiré exciton states observed in closely aligned WSe<sub>2</sub>/WS<sub>2</sub> heterostructure.<sup>[30]</sup> Reflection contrast spectra of a WSe<sub>2</sub>/WS<sub>2</sub> heterostructure with a

small twist angle and a large twist angle are shown in Figure 6b. The latter only shows a single resonance in the energy range of 1.6–1.8 eV from the WSe<sub>2</sub> A exciton state. In contrast, the moiré superlattice formed in the small angle-twisted heterostructures brings about three prominent peaks (labeled I to III), which have comparable oscillator strength in this range, corresponding to distinct moiré exciton states. Moreover, its gate dependencies are different from that of the A exciton in the WSe<sub>2</sub> monolayer and the WSe<sub>2</sub>/WS<sub>2</sub> heterostructure with a large twist angle (Figure 6c). These unusual dependencies that vary for different peaks cannot be explained by any established electron–electron

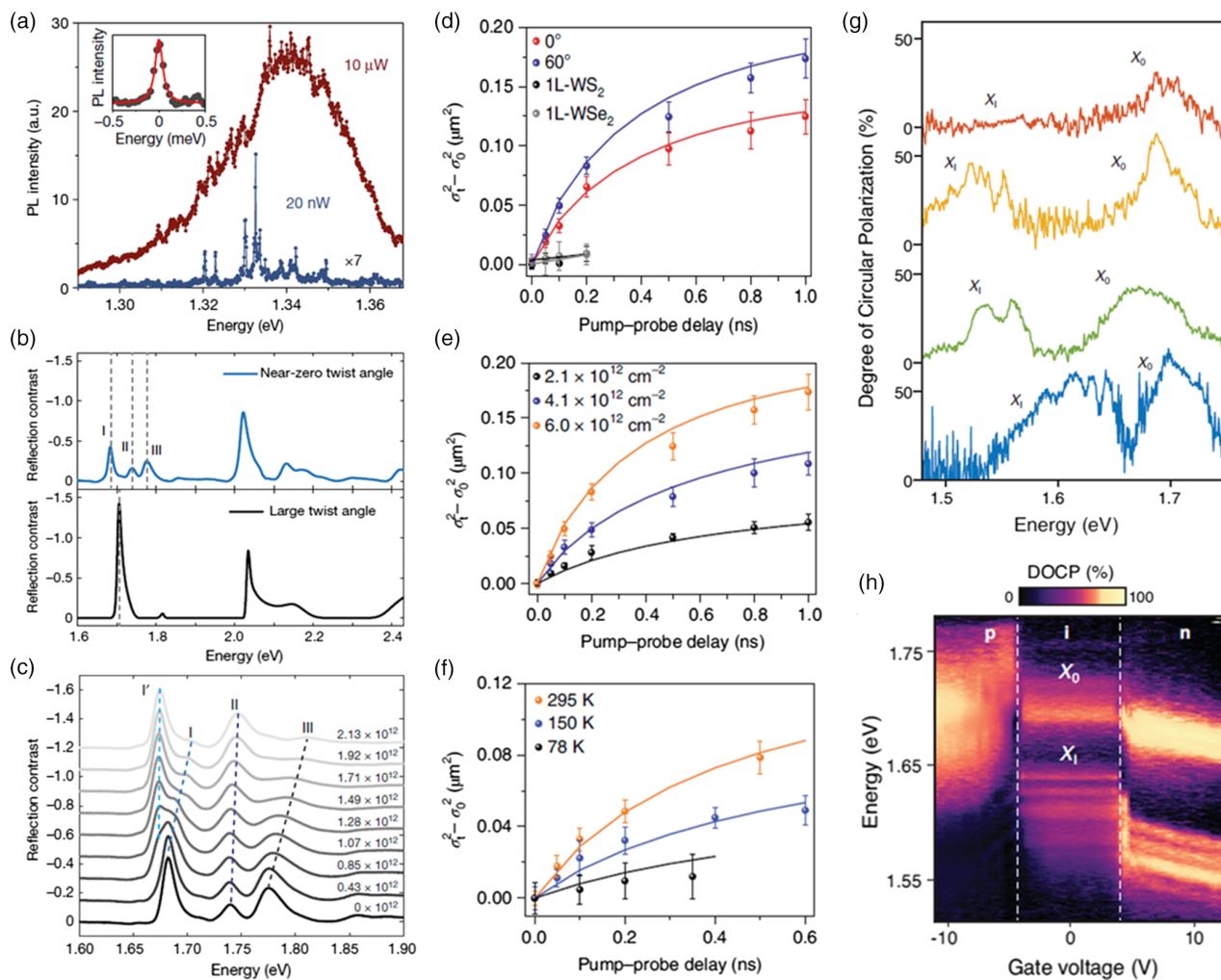


**Figure 6.** Investigation of interlayer excitons in t-TMDs. a) PL spectrum of MoSe<sub>2</sub>/WSe<sub>2</sub> heterobilayers with the twist angle of 2° at excitation powers of 10 μW (dark red) and 20 nW (blue). The inset shows the Lorentzian fit to a representative PL peak indicating a linewidth of about 100 μeV (20 nW excitation power). Reproduced with permission.<sup>[69]</sup> Copyright 2019, Springer Nature. b) Reflection contrast spectra of a WSe<sub>2</sub>/WS<sub>2</sub> heterostructure with a small twist angle (light blue, top) and one with a large twist angle (black, bottom). c) Detailed reflection contrast spectra in the range of 1.6–1.9 eV (the WSe<sub>2</sub> A exciton) on the electron-doping side. Units of the electron concentration: cm<sup>-2</sup>. b,c) Reproduced with permission.<sup>[30]</sup> Copyright 2019, Springer Nature. d) Anomalous diffusion of interlayer excitons arising from the interplay between the moiré potentials and strong many-body interactions. Twist-angle-dependent width  $\sigma_x^2 - \sigma_0^2$  with respect to the pump–probe delay times with  $N_0 = 6.0 \times 10^{12} \text{ cm}^{-2}$  at 295 K, indicating a faster transport in the 60° heterobilayer. e) Interlayer exciton transport of the 60° heterobilayer at different exciton densities at 295 K. f) Temperature-dependent interlayer exciton transport of the 60° heterobilayer with  $N_0 = 4.1 \times 10^{12} \text{ cm}^{-2}$ . d–f) Reproduced with permission.<sup>[31]</sup> Copyright 2020, Springer Nature. g) DOCP of the t-WSe<sub>2</sub> bilayers with twist angles of 180°, 0°, 2°, 17°, respectively (from top to bottom). h) The doping dependence of DOCP. Switching from large values (>80%) in the n-doped regime to almost zero (<5%) in the p-doped regime is displayed. g,h) Reproduced with permission.<sup>[54]</sup> Copyright 2020, American Physical Society.

interactions. Instead, they can be understood through an empirical theory that introduces periodic moiré exciton potential in the strong-coupling regime<sup>[83]</sup> because the interlayer electron–exciton interaction can be sufficiently enhanced by the moiré superlattice. The multiple flat bands with substantially reduced bandwidth generated in this model also provide a promising platform to explore exotic states, such as a topological exciton insulator and a strongly correlated exciton Hubbard model.<sup>[30]</sup>

Apart from the WSe<sub>2</sub>/WS<sub>2</sub> heterostructure, twist-angle-dependent interlayer exciton emission was observed in the bilayer WS<sub>2</sub>/MoS<sub>2</sub> heterostructure as well.<sup>[84]</sup> A noticeable interlayer exciton peak at around 1.5 eV can be observed in the PL spectra of coherent WS<sub>2</sub>/MoS<sub>2</sub>, whereas no peak was found in the artificially stacked random WS<sub>2</sub>/MoS<sub>2</sub>. The interlayer transition is responsible for the emission, which is suppressed in the random stacks due to nonradiative recombinations by momentum mismatch or interfacial impurity centers.

More recently, precise control of the interlayer twist angle in large-scale MoS<sub>2</sub> homostructures has been realized by Liao et al. with the stacking method.<sup>[85]</sup> The PL results demonstrate that the energies of indirect interlayer excitons can be tuned by precisely controlling the twist angles. This work introduces a pathway to industrial applications of t-TMD photonics.

#### 4.2. Diffusion of Interlayer Exciton

To further understand how the moiré landscapes modulate the properties of t-TMDs, several research works focused on exciton motions in moiré superlattices. Using transient absorption microscopy (TAM) combined with first-principles calculations, Yuan et al. investigated interlayer exciton dynamics and transport in WS<sub>2</sub>/WSe<sub>2</sub> heterobilayers with different twist angles (0° and 60°).<sup>[31]</sup> First-principle calculations indicate that moiré potentials of 0° are much deeper than those of 60° and  $\Delta E_{K-Q}$  (the mean difference of the spatial variation of the energy difference between the K–Q and the K–K transitions over the entire moiré pattern) is larger for 0° than for 60°. Therefore, the interlayer excitons in 60° samples are more mobile accordingly (Figure 6d). The migration speed of interlayer excitons is also faster at higher densities, as shown in Figure 6e, which can be explained by the net repulsive Coulomb interaction between the interlayer excitons attributed to electron–hole separation and the aligned electric dipole moments.<sup>[73,86,87]</sup> Moreover, as the temperature decreases, a reduced migration speed of exciton is observed (Figure 6f), which is of opposite tendency to intralayer excitons. These results serve as a guideline for the investigation of exciton and spin transport in vdW heterostructures and shine light on designing quantum photonics communication devices.<sup>[31]</sup>

The valley dynamics of t-TMDs have been proved to be magnificently tunable via twist angles and electrostatic doping by Scuri et al.<sup>[54]</sup> They investigated twisted WSe<sub>2</sub> (t-WSe<sub>2</sub>) bilayers with a twist angle of 0° to 17°. It was found that in contrast to the almost zero degree of circular polarization (DOCP) of a neutral interlayer exciton in natural bilayers (180°), as high as 60% can be reached in twisted bilayers upon illumination with circularly polarized light (Figure 6g). In addition, due to nondegenerate spin at K and Q points and indirection in both real and

momentum space, t-WSe<sub>2</sub> is characterized by slow depolarization and long valley lifetimes.<sup>[28,88–90]</sup> The doping dependence of DOCP is shown in Figure 6h. Although the interlayer exciton DOCP exceeds 80% in the n-doped regime, it can be switched to almost zero (<5%) in the p-doped regime. This study demonstrates the possibility to build tunable chiral photonics and electrically switchable spin–valley-based devices with t-TMD bilayers and opens up avenues for applications in quantum information storage and processing.<sup>[54]</sup>

#### 4.3. Correlated Electronic Phases

t-TMDs exhibit different electronic properties from their non-twisted counterparts as well. Recent studies have shown that the charge mobility in 30° twisted MoS<sub>2</sub> bilayers is higher than the 0° structures, manifesting as a larger on/off ratio of devices fabricated by 30° twisted bilayers.<sup>[85]</sup> Interlayer decoupling by incommensurate structure or smaller interlayer resistance may cause this phenomenon.<sup>[85,91]</sup>

Similarly to TBG, t-TMDs also provide an ideal platform for band engineering. Flat bands whose bandwidths vary continuously with the inverse moiré wavelengths and van Hove singularities (vHSs) of the moiré Brillouin zone that may support the emergent electronic phases have been predicted to exist.<sup>[15,92–95]</sup> Regarding this, Wang et al. have specially looked into the t-WSe<sub>2</sub> bilayers.<sup>[70]</sup> A schematic diagram of the band structure of t-WSe<sub>2</sub> is shown in Figure 7a. Carrier correlations are strong enough within these low-energy flat bands to induce a correlation-driven insulation state near half-filling (Figure 7b). They also observed a potential superconducting transition at low temperature away from half-filling (Figure 7c), though the superconductor gap seems to be weakly formed. A phase diagram for the t-WSe<sub>2</sub> bilayer with respect to angle and displacement field is shown in Figure 7d. According to single-particle band-structure calculations (Figure 7e), its qualitative correlation with the density of states (DOS) at half-filling indicates that the DOS at half-filling plays a key role in stabilizing the entire measured angle range. Due to its widely tunable electronic structure, the t-WSe<sub>2</sub> system with engineered flat bands can be generalized as a model system for exploring other emerging electronic phases, such as exciton condensates, spin liquids, and magnetic ordering.<sup>[70]</sup>

### 5. Conclusion

In this review, a comprehensive overview of the state-of-the-art research activities in the preparation of t-TMDs and their intriguing properties is provided. The reported synthesis conditions of twisted-bilayer MoS<sub>2</sub>, MoSe<sub>2</sub>, WS<sub>2</sub>, W-doped MoSe<sub>2</sub>, and WSe<sub>2</sub>/WS<sub>2</sub> heterostructures are summarized and discussed. Two major synthetic routes, i.e., the two-step stacking method and one-step CVD method, are introduced and compared. The stacking method is advantageous in controlling the twist angle, whereas an additional annealing step is required to eliminate the polymer residues during the transferring process. On the contrary, the CVD method offers opportunities to directly grow much cleaner t-TMD bilayers; however, the twist angle produced is random and unpredictable. Establishing the correlation between CVD synthesis parameters and the twist angles of as-grown TMD bilayers

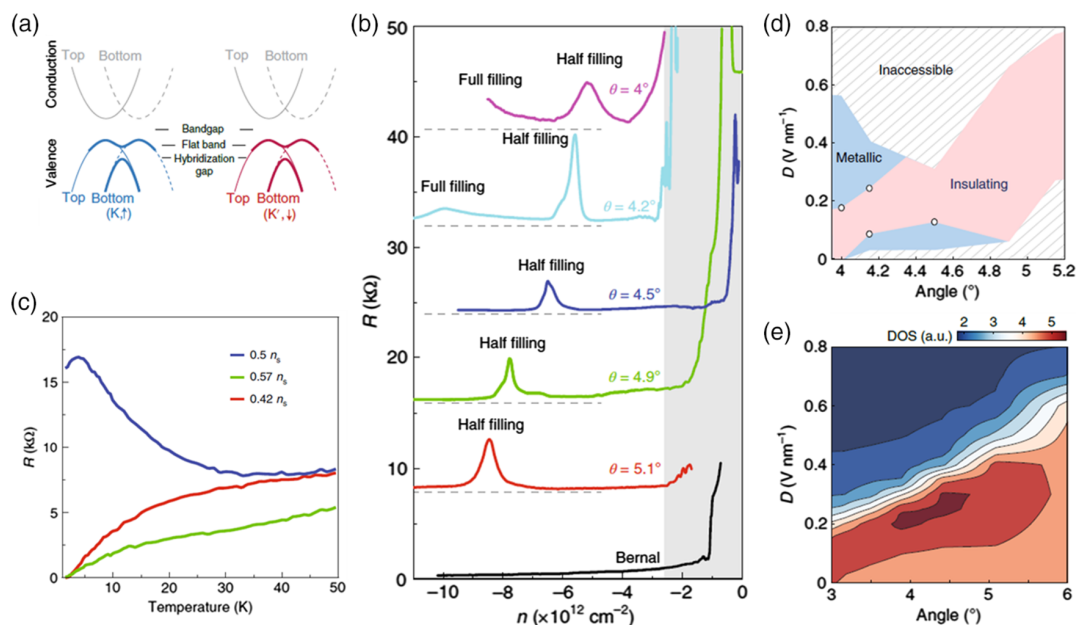


**Figure 7.** Study of correlated electronic phases of t-TMDs. a) Schematic illustration of the hybridized band structure of t-WSe<sub>2</sub> bilayers in the K valley, spin up (left), and K' valley, spin down (right). b) Resistance as a function of carrier density of bilayer WSe<sub>2</sub> with six different configurations, measured at  $T = 1.8$  K. c) Temperature-dependent resistance of bilayer WSe<sub>2</sub> with a twist angle of 5.1° at densities near half-filling. At temperatures below 35 K, the insulating response is identified at half-filling (blue). At temperatures below 3 K, zero resistance in the vicinity of half-filling (red and green) is observed. d) Phase diagram of the t-WSe<sub>2</sub> with respect to displacement field and twist angle, revealing the observed metallic and insulating regions at half-filling. White circles indicate the metal-to-insulator transitions. e) Calculated DOS at half-filling as a function of the displacement field and twist angle. Reproduced with permission.<sup>[70]</sup> Copyright 2020, Springer Nature.

would be a valuable yet challenging future research direction. Notably, the success of synthesizing the “magic” angle TBG by the “tear-and-stack” technique provides a promising direction for the controllable synthesis and study of t-TMDs, especially at small twisted angles. The introduction of non-Euclidean surfaces into the CVD growth process to prepare supertwisted TMDs offers new possibilities to construct and study t-TMDs.

In addition, as the most commonly used characterization techniques to probe the interlayer coupling between the twisted bilayers, Raman spectroscopy and PL spectroscopy are particularly elaborated on. Several intriguing physical properties identified in t-TMDs, including moiré superlattices, interlayer excitons, and correlated electronic phases, are summarized. Along with the more in-depth exploration of the twisted multilayer TMDs, more novel properties and new phenomena may arise from this intriguing structure. To realize practical optoelectronic applications, more research efforts are required to address issues related to twist-angle-controlled high-quality synthesis and comprehensive characterization.

## Acknowledgements

This work was supported by National Research Foundation Singapore program NRF-CRP21-2018-0007 and NRF-CRP22-2019-0007, Singapore Ministry of Education via AcRF Tier 3 Programme “Geometrical Quantum Materials” (MOE2018-T3-1-002), AcRF Tier 2 (MOE2016-T2-1-131) and AcRF Tier 1 RG4/17 and RG7/18. This research was also supported by A\*STAR under its AME IRG Grant (Project No. 19283074). The authors also gratefully acknowledge the support from the National Nature

Science Foundation of China (Grant No. 51771224, and 61888102) and the National Key R&D Program of China (Grant No. 2016YFA0202301 and 2018FYA0305800).

## Conflict of Interest

The authors declare no conflict of interest.

## Keywords

chemical vapor deposition, stacking method, transition metal dichalcogenides, twisted bilayers, 2D

Received: December 30, 2020  
Revised: February 9, 2021  
Published online: March 10, 2021

- [1] Q. H. Wang, K. Kalantar-Zadeh, A. Kis, J. N. Coleman, M. S. Strano, *Nat. Nanotechnol.* **2012**, *7*, 699.
- [2] Y. Chen, Z. Fan, Z. Zhang, W. Niu, C. Li, N. Yang, B. Chen, H. Zhang, *Chem. Rev.* **2018**, *118*, 6409.
- [3] M. Chhowalla, H. S. Shin, G. Eda, L.-J. Li, K. P. Loh, H. Zhang, *Nat. Chem.* **2013**, *5*, 263.
- [4] X. Zhang, H. Nan, S. Xiao, X. Wan, X. Gu, A. Du, Z. Ni, K. K. Ostrikov, *Nat. Commun.* **2019**, *10*, 598.
- [5] S. Kim, A. Konar, W.-S. Hwang, J. H. Lee, J. Lee, J. Yang, C. Jung, H. Kim, J.-B. Yoo, J.-Y. Choi, *Nat. Commun.* **2012**, *3*, 1011.
- [6] C. Long, Y. Dai, Z.-R. Gong, H. Jin, *Phys. Rev. B* **2019**, *99*, 115316.

- [7] A. Luican, G. Li, A. Reina, J. Kong, R. Nair, K. S. Novoselov, A. K. Geim, E. Andrei, *Phys. Rev. Lett.* **2011**, *106*, 126802.
- [8] G. Li, A. Luican, J. L. Dos Santos, A. C. Neto, A. Reina, J. Kong, E. Andrei, *Nat. Phys.* **2010**, *6*, 109.
- [9] M. Yankowitz, J. Xue, D. Cormode, J. D. Sanchez-Yamagishi, K. Watanabe, T. Taniguchi, P. Jarillo-Herrero, P. Jacquod, B. J. LeRoy, *Nat. Phys.* **2012**, *8*, 382.
- [10] K. S. Novoselov, E. McCann, S. Morozov, V. I. Fal'ko, M. Katsnelson, U. Zeitler, D. Jiang, F. Schedin, A. Geim, *Nat. Phys.* **2006**, *2*, 177.
- [11] C. R. Dean, L. Wang, P. Maher, C. Forsythe, F. Ghahari, Y. Gao, J. Katoch, M. Ishigami, P. Moon, M. Koshino, *Nature* **2013**, *497*, 598.
- [12] L. Ponomarenko, R. Gorbachev, G. Yu, D. Elias, R. Jalil, A. Patel, A. Mishchenko, A. Mayorov, C. Woods, J. Wallbank, *Nature* **2013**, *497*, 594.
- [13] Y. Cao, V. Fatemi, S. Fang, K. Watanabe, T. Taniguchi, E. Kaxiras, P. Jarillo-Herrero, *Nature* **2018**, *556*, 43.
- [14] Y. Cao, V. Fatemi, A. Demir, S. Fang, S. L. Tomarken, J. Y. Luo, J. D. Sanchez-Yamagishi, K. Watanabe, T. Taniguchi, E. Kaxiras, *Nature* **2018**, *556*, 80.
- [15] F. Wu, T. Lovorn, E. Tutuc, I. Martin, A. MacDonald, *Phys. Rev. Lett.* **2019**, *122*, 086402.
- [16] Z. Shi, X. Wang, Y. Sun, Y. Li, L. Zhang, *Semicond. Sci. Technol.* **2018**, *33*, 093001.
- [17] M. Yankowitz, S. Chen, H. Polshyn, Y. Zhang, K. Watanabe, T. Taniguchi, D. Graf, A. F. Young, C. R. Dean, *Science* **2019**, *363*, 1059.
- [18] K. Kim, A. DaSilva, S. Huang, B. Fallahzad, S. Larentis, T. Taniguchi, K. Watanabe, B. J. LeRoy, A. H. MacDonald, E. Tutuc, *Proc. Natl. Acad. Sci.* **2017**, *114*, 3364.
- [19] J. Zhou, J. Lin, X. Huang, Y. Zhou, Y. Chen, J. Xia, H. Wang, Y. Xie, H. Yu, J. Lei, *Nature* **2018**, *556*, 355.
- [20] X. Huang, Z. Zeng, H. Zhang, *Chem. Soc. Rev.* **2013**, *42*, 1934.
- [21] X. Duan, C. Wang, A. Pan, R. Yu, X. Duan, *Chem. Soc. Rev.* **2015**, *44*, 8859.
- [22] S. Manzeli, D. Ovchinnikov, D. Pasquier, O. V. Yazyev, A. Kis, *Nat. Rev. Mater.* **2017**, *2*, 17033.
- [23] D. Voiry, A. Mohite, M. Chhowalla, *Chem. Soc. Rev.* **2015**, *44*, 2702.
- [24] K. Chen, X. Wan, J. Xu, *Adv. Funct. Mater.* **2017**, *27*, 1603884.
- [25] J. Zhou, B. Tang, J. Lin, D. Lv, J. Shi, L. Sun, Q. Zeng, L. Niu, F. Liu, X. Wang, *Adv. Funct. Mater.* **2018**, *28*, 1801568.
- [26] P. K. Sahoo, S. Memaran, Y. Xin, L. Balicas, H. R. Gutiérrez, *Nature* **2018**, *553*, 63.
- [27] A. M. Jones, H. Yu, J. S. Ross, P. Klement, N. J. Ghimire, J. Yan, D. G. Mandrus, W. Yao, X. Xu, *Nat. Phys.* **2014**, *10*, 130.
- [28] F. Wu, T. Lovorn, A. MacDonald, *Phys. Rev. B* **2018**, *97*, 035306.
- [29] J. Sung, Y. Zhou, G. Scuri, V. Zólyomi, T. I. Andersen, H. Yoo, D. S. Wild, A. Y. Joe, R. J. Gelly, H. Heo, S. J. Magorrian, D. Bérubé, A. M. M. Valdivia, T. Taniguchi, K. Watanabe, M. D. Lukin, P. Kim, V. I. Fal'ko, H. Park, *Nat. Nanotechnol.* **2020**, *15*, 750.
- [30] C. Jin, E. C. Regan, A. Yan, M. I. B. Utama, D. Wang, S. Zhao, Y. Qin, S. Yang, Z. Zheng, S. Shi, *Nature* **2019**, *567*, 76.
- [31] L. Yuan, B. Zheng, J. Kunstmann, T. Brumme, A. B. Kuc, C. Ma, S. Deng, D. Blach, A. Pan, L. Huang, *Nat. Mater.* **2020**, *19*, 671.
- [32] S. Huang, X. Ling, L. Liang, J. Kong, H. Terrones, V. Meunier, M. S. Dresselhaus, *Nano Lett.* **2014**, *14*, 5500.
- [33] A. Bachmatiuk, R. Abelin, H. T. Quang, B. Trzebicka, J. Eckert, M. H. Rummeli, *Nanotechnology* **2014**, *25*, 365603.
- [34] K. Liu, L. Zhang, T. Cao, C. Jin, D. Qiu, Q. Zhou, A. Zettl, P. Yang, S. G. Louie, F. Wang, *Nat. Commun.* **2014**, *5*, 4966.
- [35] S. Zheng, L. Sun, X. Zhou, F. Liu, Z. Liu, Z. Shen, H. J. Fan, *Adv. Opt. Mater.* **2015**, *3*, 1600.
- [36] K. Wang, B. Huang, M. Tian, F. Ceballos, M.-W. Lin, M. Mahjouri-Samani, A. Boulesbaa, A. A. Puzos, C. M. Rouleau, M. Yoon, *ACS Nano* **2016**, *10*, 6612.
- [37] A. A. Puzos, L. Liang, X. Li, K. Xiao, B. G. Sumpter, V. Meunier, D. B. Geohegan, *ACS Nano* **2016**, *10*, 2736.
- [38] S. A. Han, R. Bhatia, S.-W. Kim, *Nano Convergence* **2015**, *2*, 17.
- [39] Y. Shi, H. Li, L.-J. Li, *Chem. Soc. Rev.* **2015**, *44*, 2744.
- [40] Q. Ji, Y. Zhang, Y. Zhang, Z. Liu, *Chem. Soc. Rev.* **2015**, *44*, 2587.
- [41] Z. Cai, B. Liu, X. Zou, H.-M. Cheng, *Chem. Rev.* **2018**, *118*, 6091.
- [42] S. Y. Kim, J. Kwak, C. V. Ciobanu, S. Y. Kwon, *Adv. Mater.* **2019**, *31*, 1804939.
- [43] H. Li, Y. Li, A. Aljarb, Y. Shi, L.-J. Li, *Chem. Rev.* **2017**, *118*, 6134.
- [44] Y. Huang, Y.-H. Pan, R. Yang, L.-H. Bao, L. Meng, H.-L. Luo, Y.-Q. Cai, G.-D. Liu, W.-J. Zhao, Z. Zhou, *Nat. Commun.* **2020**, *11*, 2453.
- [45] X. Ma, Q. Liu, D. Xu, Y. Zhu, S. Kim, Y. Cui, L. Zhong, M. Liu, *Nano Lett.* **2017**, *17*, 6961.
- [46] L. Tao, H. Li, Y. Gao, Z. Chen, L. Wang, Y. Deng, J. Zhang, J. B. Xu, *Adv. Mater. Technol.* **2018**, *3*, 1700282.
- [47] M.-L. Lin, Q.-H. Tan, J.-B. Wu, X.-S. Chen, J.-H. Wang, Y.-H. Pan, X. Zhang, X. Cong, J. Zhang, W. Ji, *ACS Nano* **2018**, *12*, 8770.
- [48] J. C. Shaw, H. Zhou, Y. Chen, N. O. Weiss, Y. Liu, Y. Huang, X. Duan, *Nano Res.* **2014**, *7*, 511.
- [49] S. V. Mandyam, M.-Q. Zhao, P. Masih Das, Q. Zhang, C. C. Price, Z. Gao, V. B. Shenoy, M. Drndic, A. T. C. Johnson, *ACS Nano* **2019**, *13*, 10490.
- [50] Y. Zhao, C. Zhang, D. D. Kohler, J. M. Scheeler, J. C. Wright, P. M. Voyles, S. Jin, *Science* **2020**, *370*, 442.
- [51] A. Uri, S. Grover, Y. Cao, J. Crosse, K. Bagani, D. Rodan-Legrain, Y. Myasoedov, K. Watanabe, T. Taniguchi, P. Moon, *Nature* **2020**, *581*, 47.
- [52] Y. Cao, J. Luo, V. Fatemi, S. Fang, J. Sanchez-Yamagishi, K. Watanabe, T. Taniguchi, E. Kaxiras, P. Jarillo-Herrero, *Phys. Rev. Lett.* **2016**, *117*, 116804.
- [53] K. Kim, M. Yankowitz, B. Fallahzad, S. Kang, H. C. Movva, S. Huang, S. Larentis, C. M. Corbet, T. Taniguchi, K. Watanabe, *Nano Lett.* **2016**, *16*, 1989.
- [54] G. Scuri, T. I. Andersen, Y. Zhou, D. S. Wild, J. Sung, R. J. Gelly, D. Bérubé, H. Heo, L. Shao, A. Y. Joe, *Phys. Rev. Lett.* **2020**, *124*, 217403.
- [55] H. Chen, X.-L. Zhang, Y.-Y. Zhang, D. Wang, D.-L. Bao, Y. Que, W. Xiao, S. Du, M. Ouyang, S. T. Pantelides, *Science* **2019**, *365*, 1036.
- [56] X. Zhang, X.-F. Qiao, W. Shi, J.-B. Wu, D.-S. Jiang, P.-H. Tan, *Chem. Soc. Rev.* **2015**, *44*, 2757.
- [57] H. R. Gutiérrez, N. Perea-López, A. L. Elías, A. Berkdemir, B. Wang, R. Lv, F. López-Urías, V. H. Crespi, H. Terrones, M. Terrones, *Nano Lett.* **2013**, *13*, 3447.
- [58] W. Zhao, Z. Ghorannevis, L. Chu, M. Toh, C. Kloc, P.-H. Tan, G. Eda, *ACS Nano* **2013**, *7*, 791.
- [59] A. Berkdemir, H. R. Gutiérrez, A. R. Botello-Méndez, N. Perea-López, A. L. Elías, C.-I. Chia, B. Wang, V. H. Crespi, F. López-Urías, J.-C. Charlier, *Sci. Rep.* **2013**, *3*, 1755.
- [60] G. R. Bhimanapati, Z. Lin, V. Meunier, Y. Jung, J. Cha, S. Das, D. Xiao, Y. Son, M. S. Strano, V. R. Cooper, *ACS Nano* **2015**, *9*, 11509.
- [61] H. Zeng, B. Zhu, K. Liu, J. Fan, X. Cui, Q. Zhang, *Phys. Rev. B* **2012**, *86*, 241301.
- [62] P. Tan, W. Han, W. Zhao, Z. Wu, K. Chang, H. Wang, Y. Wang, N. Bonini, N. Marzari, N. Pugno, *Nat. Mater.* **2012**, *11*, 294.
- [63] J.-B. Wu, X. Zhang, M. Ijäs, W.-P. Han, X.-F. Qiao, X.-L. Li, D.-S. Jiang, A. C. Ferrari, P.-H. Tan, *Nat. Commun.* **2014**, *5*, 5309.
- [64] S. Huang, L. Liang, X. Ling, A. A. Puzos, D. B. Geohegan, B. G. Sumpter, J. Kong, V. Meunier, M. S. Dresselhaus, *Nano Lett.* **2016**, *16*, 1435.
- [65] J. Kang, J. Li, S.-S. Li, J.-B. Xia, L.-W. Wang, *Nano Lett.* **2013**, *13*, 5485.
- [66] B. Hunt, J. D. Sanchez-Yamagishi, A. F. Young, M. Yankowitz, B. J. LeRoy, K. Watanabe, T. Taniguchi, P. Moon, M. Koshino, P. Jarillo-Herrero, *Science* **2013**, *340*, 1427.

- [67] G. Chen, L. Jiang, S. Wu, B. Lyu, H. Li, B. L. Chittari, K. Watanabe, T. Taniguchi, Z. Shi, J. Jung, *Nat. Phys.* **2019**, *15*, 237.
- [68] W. Choi, I. Akhtar, M. A. Rehman, M. Kim, D. Kang, J. Jung, Y. Myung, J. Kim, H. Cheong, Y. Seo, *ACS Appl. Mater. Interfaces* **2018**, *11*, 2470.
- [69] K. L. Seyler, P. Rivera, H. Yu, N. P. Wilson, E. L. Ray, D. G. Mandrus, J. Yan, W. Yao, X. Xu, *Nature* **2019**, *567*, 66.
- [70] L. Wang, E.-M. Shih, A. Ghiotto, L. Xian, D. A. Rhodes, C. Tan, M. Claassen, D. M. Kennes, Y. Bai, B. Kim, *Nat. Mater.* **2020**, *19*, 861.
- [71] H. Yu, Y. Wang, Q. Tong, X. Xu, W. Yao, *Phys. Rev. Lett.* **2015**, *115*, 187002.
- [72] H. Yu, G.-B. Liu, J. Tang, X. Xu, W. Yao, *Sci. Adv.* **2017**, *3*, e1701696.
- [73] P. Rivera, K. L. Seyler, H. Yu, J. R. Schaibley, J. Yan, D. G. Mandrus, W. Yao, X. Xu, *Science* **2016**, *351*, 688.
- [74] P. Nagler, M. V. Ballottin, A. A. Mitioglu, F. Mooshammer, N. Paradiso, C. Strunk, R. Huber, A. Chernikov, P. C. Christianen, C. Schüller, *Nat. Commun.* **2017**, *8*, 1551.
- [75] C. Jiang, W. Xu, A. Rasmita, Z. Huang, K. Li, Q. Xiong, W.-b. Gao, *Nat. Commun.* **2018**, *9*, 753.
- [76] W.-T. Hsu, L.-S. Lu, P.-H. Wu, M.-H. Lee, P.-J. Chen, P.-Y. Wu, Y.-C. Chou, H.-T. Jeng, L.-J. Li, M.-W. Chu, *Nat. Commun.* **2018**, *9*, 1356.
- [77] A. Ciarrocchi, D. Unuchek, A. Avsar, K. Watanabe, T. Taniguchi, A. Kis, *Nat. Photonics* **2019**, *13*, 131.
- [78] K. Tran, G. Moody, F. Wu, X. Lu, J. Choi, K. Kim, A. Rai, D. A. Sanchez, J. Quan, A. Singh, *Nature* **2019**, *567*, 71.
- [79] P. Rivera, J. R. Schaibley, A. M. Jones, J. S. Ross, S. Wu, G. Aivazian, P. Klement, K. Seyler, G. Clark, N. J. Ghimire, *Nat. Commun.* **2015**, *6*, 6242.
- [80] P. Nagler, G. Plechinger, M. V. Ballottin, A. Mitioglu, S. Meier, N. Paradiso, C. Strunk, A. Chernikov, P. C. Christianen, C. Schüller, *2D Mater.* **2017**, *4*, 025112.
- [81] B. Miller, A. Steinhoff, B. Pano, J. Klein, F. Jahnke, A. Holleitner, U. Wurstbauer, *Nano Lett.* **2017**, *17*, 5229.
- [82] J. S. Ross, P. Rivera, J. Schaibley, E. Lee-Wong, H. Yu, T. Taniguchi, K. Watanabe, J. Yan, D. Mandrus, D. Cobden, *Nano Lett.* **2017**, *17*, 638.
- [83] F. Wu, T. Lovorn, A. H. MacDonald, *Phys. Rev. Lett.* **2017**, *118*, 147401.
- [84] H. Heo, J. H. Sung, S. Cha, B.-G. Jang, J.-Y. Kim, G. Jin, D. Lee, J.-H. Ahn, M.-J. Lee, J. H. Shim, *Nat. Commun.* **2015**, *6*, 7372.
- [85] M. Liao, Z. Wei, L. Du, Q. Wang, J. Tang, H. Yu, F. Wu, J. Zhao, X. Xu, B. Han, *Nat. Commun.* **2020**, *11*, 2153.
- [86] L. A. Jauregui, A. Y. Joe, K. Pistunova, D. S. Wild, A. A. High, Y. Zhou, G. Scuri, K. De Greve, A. Sushko, C.-H. Yu, *Science* **2019**, *366*, 870.
- [87] D. Unuchek, A. Ciarrocchi, A. Avsar, Z. Sun, K. Watanabe, T. Taniguchi, A. Kis, *Nat. Nanotechnol.* **2019**, *14*, 1104.
- [88] A. Kormányos, V. Zólyomi, V. I. Fal'ko, G. Burkard, *Phys. Rev. B* **2018**, *98*, 035408.
- [89] J. R. Schaibley, H. Yu, G. Clark, P. Rivera, J. S. Ross, K. L. Seyler, W. Yao, X. Xu, *Nat. Rev. Mater.* **2016**, *1*.
- [90] P. Rivera, H. Yu, K. L. Seyler, N. P. Wilson, W. Yao, X. Xu, *Nat. Nanotechnol.* **2018**, *13*, 1004.
- [91] K. Zhou, D. Wickramaratne, S. Ge, S. Su, A. De, R. K. Lake, *Phys. Chem. Chem. Phys.* **2017**, *19*, 10406.
- [92] F. Wu, T. Lovorn, E. Tutuc, A. H. MacDonald, *Phys. Rev. Lett.* **2018**, *121*, 026402.
- [93] M. H. Naik, M. Jain, *Phys. Rev. Lett.* **2018**, *121*, 266401.
- [94] D. A. Ruiz-Tijerina, V. I. Fal'ko, *Phys. Rev. B* **2019**, *99*, 125424.
- [95] C. Schrade, L. Fu, *Phys. Rev. B* **2019**, *100*, 035413.



**Bijun Tang** received her B.E. degree from Nanyang Technological University (NTU), Singapore, with First Class Honours (2017). She is currently pursuing a Ph.D. degree under the supervision of Prof. Zheng Liu at the School of Materials Science and Engineering, NTU. Her research interests mainly focus on the synthesis and exploration of novel 2D materials.



**Haitao Yang** is an associate professor at the Institute of Physics, Chinese Academy of Sciences. He completed his Ph.D. at the Institute of Physics and then worked in Prof. Migaku Takahashi's group as a JSPS postdoctorate research fellow at Tohoku University. He also worked in Prof. Shouheng Sun's group as a visiting scholar (2016) at Brown University. His current research interests focus on the growth and physical properties of low-dimensional materials.



**Jiadong Zhou** is a professor at the Beijing Institute of Technology. He received his B.S degree (2009) at Shaanxi University of Science & Technology, M.S. degree (2013) at Shanghai Institute of Ceramics, Chinese Academy of Sciences, and completed his Ph.D. (2017) at NTU, Singapore. He then worked as a postdoctorate research fellow at the School of Materials Science and Engineering, NTU. His current research interests focus on the synthesis, characterizations, and applications of novel 2D crystals.





**Zheng Liu** is an associate professor at the School of Materials Science and Engineering, NTU. He received his B.S. degrees (2005) at Nankai University (China) and completed his Ph.D. at the National Center for Nanoscience and Technology (NCNST), China. He then worked in Prof. Pulickel M. Ajayan and Prof. Jun Lou's groups as a joint postdoctorate research fellow (2010–2012) and research scientist (2012–2013) at Rice University. His current research interests focus on the growth and applications of 2D materials with only single-atom thickness, via innovative methods and artificial intelligence technology.